HHS Public Access

Author manuscript

Nat Immunol. Author manuscript; available in PMC 2024 March 06.

Published in final edited form as:

Nat Immunol. 2023 February ; 24(2): 320–336. doi:10.1038/s41590-022-01402-z.

Enhancer-instructed epigenetic landscape and chromatin compartmentalization dictate a primary antibody repertoire protective against specific bacterial pathogens

E. Mauricio Barajas-Mora[1], **Lindsay Lee**[2], **Hanbin Lu**[1], **J. Andrés Valderrama**[3], **Elisabet Bjanes**[3], **Victor Nizet**[3,4], **Ann J. Feeney**[5], **Ming Hu**[2,✉], **Cornelis Murre**[1,✉]

[1]Department of Molecular Biology, University of California, San Diego, La Jolla, CA, USA.

[2]Department of Quantitative Health Sciences, Lerner Research Institute, Cleveland Clinic Foundation, Cleveland, OH, USA.

[3]Department of Pediatrics, University of California, San Diego, La Jolla, CA, USA.

[4]Skaggs School of Pharmacy and Pharmaceutical Sciences, University of California, San Diego, La Jolla, USA.

[5]Department of Immunology and Microbiology, Scripps Research, La Jolla, CA, USA.

Abstract

Antigen receptor loci are organized into variable (V), diversity (D) and joining (J) gene segments that rearrange to generate antigen receptor repertoires. Here, we identified an enhancer (E34) in the murine immunoglobulin kappa (Igk) locus that instructed rearrangement of V_{κ} genes located in a sub-topologically associating domain, including a V_{κ} gene encoding for antibodies

✉**Correspondence and requests for materials** should be addressed to Ming Hu or Cornelis Murre. hum@ccf.org; cmurre@ucsd.edu.

Author contributions

E.M.B.-M. designed and performed experiments. L.L. and M.H. analyzed HiC data. H.L. contributed with CUT&RUN analysis. J.A.V. provided technical support. A.J.F. and V.N. provided advice. E.M.B.-M. and E.B. performed survival studies. E.M.B.-M. and C.M. prepared the manuscript with inputs from other authors. C.M. supervised the study.

Competing interests

The authors declare no competing interests.

Additional information

Extended data is available for this paper at https://doi.org/10.1038/s41590-022-01402-z.

Supplementary information The online version contains supplementary material available at https://doi.org/10.1038/s41590-022-01402-z.

Peer review information *Nature Immunology* thanks Yehudit Bergman and the other, anonymous, reviewer(s) for their contribution to the peer review of this work. L. A. Dempsey was the primary editor on this article and managed its editorial process and peer review in collaboration with the rest of the editorial team.

Reporting summary

Further information on research design is available in the Nature Portfolio Reporting Summary linked to this article.

Code availability

Software used for HiC data analysis is available at GitHub (https://github.com/ren-lab/hic-pipeline and https://github.com/aidenlab/juicer).

Online content

Any methods, additional references, Nature Portfolio reporting summaries, source data, extended data, supplementary information, acknowledgements, peer review information; details of author contributions and competing interests; and statements of data and code availability are available at https://doi.org/10.1038/s41590-022-01402-z.

targeting bacterial phosphorylcholine. We show that E34 instructs the nuclear repositioning of the E34 sub-topologically associating domain from a recombination-repressive compartment to a recombination-permissive compartment that is marked by equivalent activating histone modifications. Finally, we found that E34-instructed V_κ-J_κ rearrangement was essential to combat *Streptococcus pneumoniae* but not methicillin-resistant *Staphylococcus aureus* or influenza infections. We propose that the merging of V_κ genes with J_κ elements is instructed by one-dimensional epigenetic information imposed by enhancers across V_κ and J_κ genomic regions. The data also reveal how enhancers generate distinct antibody repertoires that provide protection against lethal bacterial infection.

B cells generate diverse antibody repertoires through somatic recombination of distinct gene segments. Antibodies are encoded by the immunoglobulin heavy chain (Igh) locus, and by the immunoglobulin kappa (Igk) or the immunoglobulin lambda (Igl) loci. The Igh locus is segregated into variable (V), diversity (D), joining (J) and constant (C) regions. The Igk and Igl loci are composed of V, J and C regions. Igh and Igl locus recombination occurs by deletion, while Igk rearrangement is mediated by deletion or inversion[1]. Immunoglobulin loci rearrangement is mediated by the Recombination-Activating gene 1 (Rag1) and Rag2 enzymes which cleave recombination signal sequences (RSSs) flanking the V, D and J gene segments[1]. During B cell development, rearrangement is mostly sequential. At the pro-B cell stage, D_H-J_H rearrangement precedes that of V_H-D_HJ_H joining. Pro-B cells that undergo V_κ gene rearrangement largely give rise to B1a cells, but the majority of V_κ-J_κ rearrangement is initiated at the pre-B cell stage[2,3]. If V_κ-J_κ rearrangement is nonproductive or auto-reactive, V_κ regions continue to recombine until a functional non-self-reactive V_κ-J_κ gene product is generated or proceeds to generate V_λ-J_λ joints[4].

Topologically associating domains (TADs) are a primary mode for higher-order chromatin structure[5,6]. TADs are evolutionarily conserved genomic regions with high internal versus external chromatin interaction frequencies. TADs tend to contain co-regulated loci[7]. Within TADs, smaller domains with similar interaction patterns, named sub-topologically associating domains (subTADs), are often present, which tend to be cell-type specific[8,9]. TADs and subTADs are formed by cohesin-dependent loop extrusion initiated across the chromatin landscape and are typically, but not always, demarcated by convergent CTCF-bound sites[10–18]. The Igh locus is organized as clusters of chromatin loops anchored by CTCF[19–21]. In the Igh locus, loop extrusion contributes to V_H-D_HJ_H rearrangement by a process that involves Rag-mediated scanning initiated at D_HJ_H joints followed by a search for compatible RSSs[22–28].

Igk locus assembly is regulated by regulatory elements, including an enhancer (iE_κ) located between the J and C regions, an enhancer ($3'E_\kappa$) positioned downstream of the C region and an enhancer (E88) that shapes the composition of the V_κ gene repertoire[29–33]. The Igk locus is assembled into clusters of chromatin loops anchored by CTCF[32,34]. In the V_κ-gene region, some of these chromatin loops can be classified as subTADs[32,34]. Two additional structural CTCF binding elements, named CER and SIS, separate the V_κ from the J_κ regions[35–37]. The CER and SIS elements restrict proximal V_κ-J_κ joining but facilitate distal V_κ rearrangements[35–37]. The SIS element is also involved in targeting the Igk alleles

to the pericentromeric heterochromatin. During the transition from the lymphoid progenitors to the pre-B cell stage, the Igk locus undergoes large-scale alterations in epigenetic marks, transcriptional profiles and chromatin folding, including the assembly of de novo CTCF-mediated loops[32,34,38,39].

Multiple mechanisms, including RSS quality, epigenetic environment, transcription factor binding, Rag-scanning and genome topology, dictate antigen receptor locus rearrangement[20,22–24,28,32,38,40,41]. However, it remains to be determined whether genome locus topology shapes antigen receptor repertoires in a manner that allows the host to target specific pathogen structures. To explore that possibility, we focused on a specific antibody named EO6/T15 that targets phosphorylcholine in bacterial phospholipids[42–45]. We identified an enhancer, named E34, located within close genomic proximity of the V_{κ} gene utilized in the EO6/T15 antibody. We generated E34-deficient (E34Δ) mice and found that the E34 enhancer instructed the assembly of an antibody repertoire directed against bacterial phosphorylcholine. We found that E34 prompted the deposition of active chromatin histone marks to reposition the E34 subTAD away from a recombination-repressive to a recombination-permissive compartment to promote intermingle with other V_{κ} genes and J_{κ} elements. E34-instructed alterations in nuclear location promoted chromatin accessibility at RSSs at V_{κ} genes that span the E34 subTAD. E34 promoted the deposition of enhancer-associated histone marks and CTCF binding across the E34 subTAD to facilitate chromatin interaction between the V_{κ} and J_{κ} genes. Finally, we found that E34-instructed V_{κ}-J_{κ} rearrangement provided protection against lethal *Streptococcus pneumoniae* infection. Conversely, the E34 enhancer did not prevent lethality when infected with methicillin-resistant *Staphylococcus aureus* (MRSA) or exposure to a lethal dose of influenza virus. Taken together, these data reveal how enhancer-instructed epigenetic reprogramming and nuclear repositioning physically pull V_{κ} and J_{κ} elements into close physical proximity to promote the generation of antibody repertoires that protect against lethal bacterial infection.

Results

An enhancer that instructs *Igkv7–33* gene rearrangement

It is now established that nuclear architecture orchestrates antigen receptor locus rearrangement. However, whether and how genome locus topology shapes the V_{κ} gene repertoire to target specific pathogen structures remains to be determined. To explore this question, we examined the Igk locus for enhancers located nearby *Igkv7–33*. *Igkv7–33* encodes for a light chain utilized in the EO6/T15 antibody that targets phosphorylcholine in bacterial phospholipids[42–45]. Specifically, we searched for sites enriched for H3K4me1 and H3K27Ac deposition nearby to *Igkv7–33*. As a result, we identified a potential enhancer, named E34, located in the vicinity of *Igkv7–33* (Extended Fig. 1a,b). We found that E34 was associated with B-cell-specific enhancer-associated transcription factors such as E2A, EBF1, IRF4, PU.1 and Pax5, as well as with histone acetyltransferases (p300), chromatin remodeler complexes (Brg1) and coactivators (Mediator) (Extended Data Fig. 1b,c)[46–48].

To determine whether E34 plays a role in V_{κ}-J_{κ} rearrangement, we generated E34Δ mice using CRISPR–Cas9-mediated genome editing (Extended Data Fig. 1b). Multiple mice were generated that carried predicted excisions (Extended Data Fig. 1d). Bone marrow cells

derived from wild-type (WT) and E34Δ mice were collected and stained for the expression of CD19, CD93, CD2, CD43 and IgM. E34Δ mice exhibited normal ratios of pro-B, large and small pre-B, immature B and recirculating B cells (Extended Data Fig. 2a). Likewise, B2, B1a and B1b B cell compartments in the peritoneal cavity were not affected in E34Δ mice (Extended Data Fig. 2b). Splenocytes in E34Δ mice showed normal follicular (Fo-B), marginal zone B (MZ-B) and transitional B (Tr-B) cell compartments (Extended Data Fig. 2c). B cell cellularity was also not affected in the bone marrow, spleen and peritoneal cavity derived from E34Δ mice (Extended Data Fig. 2d–f). Thus, deletion of E34 does not modulate B cell development.

To determine whether E34 regulates V_κ-J_κ rearrangement, we sorted pro-B and small pre-B cells from the bone marrow and B1a and B1b B cells from the peritoneal cavity. DNA and RNA libraries were generated from pre-B cells, while RNA libraries were generated for pro-B, B1a and B1b B cells. Libraries were sequenced and analyzed for V_κ-J_κ rearrangements. We found that the V_κ repertoire was affected in pre-B cells derived from E34Δ mice compared with WT mice (Fig. 1a,b). Likewise, in pro-B, B1a and B1b B cells, V_κ rearrangements involving the *Igkv7–33* gene were also impacted by deletion of the E34 enhancer (Fig. 1c and Extended Data Fig. 3a,b). E34 excision predominantly perturbed rearrangements involving nearby-located V_κ genes (Fig. 1a,b and Extended Data Fig. 3a,b). V_κ genes located beyond the affected V_κ region displayed a marginal increase in V_κ-J_κ rearrangement (Fig. 1a,b and Extended Data Fig. 3a,b). In sum, these data indicate that the E34 enhancer regulates the rearrangement of neighboring V_κ genes, including *Igkv7–33*.

The E34 enhancer instructs *Igkv7–33*-related V_κ rearrangement

V_κ genes can be categorized by genetically related families[49]. To determine whether the reduction in V_κ-J_κ rearrangement in E34Δ mice correlates with V_κ family gene relatedness, we analyzed fold changes in V_κ gene rearrangement in pre-B cells isolated from WT and E34Δ mice (Fig. 1d). We found that E34 deletion affected Igk locus rearrangements involving Igkv3 (10 V_κ genes), Igkv6 (9 V_κ genes), Igkv7 (1 V_κ gene), Igkv8 (11 V_κ genes) and Igkv18 (1 V_κ gene) families. Next, we generated a phylogenetic tree for functional V_κ genes (Fig. 1e). Three of the most significantly affected families, Igkv6, Igkv7 and Igkv8, were closely related. The level of reduced rearrangement among these V_κ families was distinct and correlated with genomic separation from E34 (Fig. 1f). Since the Igkv6, Igkv7 and Igkv8 gene families were closely related, we compared the reduction of rearrangement for all V_κ genes in these families with other V_κ genes that displayed reduced or elevated levels of rearrangement. We found that deletion of E34 distinctively affected rearrangement involving *Igkv7–33*-related V_κ genes which are located in the vicinity of E34 (Fig. 1g). Taken together, these data indicate that E34 preferentially instructs V_κ-J_κ rearrangement involving *Igkv7–33*-related V_κ gene families.

E34 instructs a distinct pattern of chromatin folding

To determine how E34 instructs V_κ-J_κ rearrangement, we generated WT and E34Δ mice that carried the Igk locus in a RAG-deficient background. WT-*Rag1*$^{-/-}$ and E34Δ-*Rag1*$^{-/-}$ mice were crossed with mice that expressed a human IgM transgene (hIgM), generating mice which in pre-B cells carry the Igk locus in a germline configuration[50]. CD19-expressing

cells from the bone marrow, consisting of >95% pre-B cells, isolated from WT-*Rag1*$^{-/-}$.hIgM and E34Δ-*Rag1*$^{-/-}$.hIgM mice were formaldehyde-fixed and analyzed using high-throughput chromosome-conformation capture (HiC). HiC is a method often used to map higher-order chromatin structure and nuclear architecture[51]. We identified >500 million paired-end reads, yielding highly reproducible biological replicates for WT-*Rag1*$^{-/-}$.hIgM and E34Δ-*Rag1*$^{-/-}$.hIgM pre-B cells (Extended Data Fig. 4a and Supplementary Table 1). Chromatin interaction frequencies, when plotted as a function of genomic distance, scaled similarly for WT-*Rag1*$^{-/-}$.hIgM and E34Δ-*Rag1*$^{-/-}$.hIgM pre-B cells (Extended Data Fig. 4b). Likewise, pre-B cells isolated from WT-*Rag1*$^{-/-}$.hIgM and E34Δ-*Rag1*$^{-/-}$.hIgM mice showed similar interaction plaid-like patterns (Extended Data Fig. 4c,d). However, differences in chromatin interaction frequencies became evident upon visualizing the data as differential contact maps (Fig. 2a, dashed rectangle). Zooming-in on the Igk locus, we found that contact frequencies involving genomic regions nearby E34 and J_{κ} elements, the CER and SIS elements, and iE_{κ} and $3'E_{\kappa}$ enhancers, hereafter collectively referred to as the Igκ RR, differed (red versus blue gradient) between WT-*Rag1*$^{-/-}$.hIgM and E34Δ-*Rag1*$^{-/-}$.hIgM pre-B cells (Fig. 2b,c, dashed square, and Extended Data Fig. 4e,f). Taken together, the E34 enhancer instructs distinct patterns of chromatin folding across the Igk locus.

E34 assembles boundary elements that define the E34 subTAD

Previous studies, as well as the data described above, suggest that the Igk locus is assembled into multiple subTADs (Fig. 2b and Extended Data Fig. 4e)[32,34,52]. To verify the presence of subTADs in statistical terms, we calculated the insulation score (IS) as well as the directionality index (DI) across the Igk locus[5,14,53]. The IS measures the strength of each genomic locus to block or insulate local interactions across the region, revealing the presence of TAD boundaries. The DI measures the bias in contact frequencies upstream and downstream of a genomic region identifying TAD boundaries. Both IS and DI, when measured stepwise across the Igk locus, revealed the presence of boundary elements that defined four subTADs in WT-*Rag1*$^{-/-}$.hIgM and E34Δ-*Rag1*$^{-/-}$. hIgM pre-B cells (Fig. 2d). We found that reversals in IS and DI correlated well with enrichment for CTCF and Rad21 occupancy, consistent with the associated genomic regions functioning as boundary elements (Fig. 2d)[5,14,53]. Notably, however, the IS and DI analysis revealed changes in subTAD boundaries between the subTAD containing the E34 enhancer (E34 subTAD) and the upstream subTAD in WT-*Rag1*$^{-/-}$. hIgM versus E34Δ-*Rag1*$^{-/-}$.hIgM pre-B cells (Fig. 2d, gray versus red dashed lines, black arrow versus red arrow). Taken together, these data indicate that the E34 enhancer instructs de novo boundary elements that define the E34 subTAD.

E34 drives interactions linking the E34 subTAD and the Igκ RR

To evaluate the significant changes in chromatin interactions between WT-*Rag1*$^{-/-}$.hIgM and E34Δ-*Rag1*$^{-/-}$.hIgM pre-B cells, we used three different methods. First, we used FitHiC2 to identify significant chromatin interactions[54]. We found that significant chromatin interactions involving a large genomic region nearby the E34 enhancer and the Igκ RR were depleted in E34Δ-*Rag1*$^{-/-}$.hIgM pre-B cells versus WT-*Rag1*$^{-/-}$. hIgM pre-B cells (Fig. 3a,b, black versus blue arrows). To determine whether these chromatin interactions were associated with architectural anchors or enhancer-associated epigenetic marks, we

plotted CTCF, Rad21, H3K4me1 and H3K27Ac chromatin immunoprecipitation sequencing reads. We found that genomic regions depleted for chromatin interactions in E34Δ-*Rag1*$^{-/-}$.hIgM pre-B cells were associated with CTCF, Rad21, H3K4me1 and H3K27Ac occupancy (Fig. 3a,b, blue highlights). Second, we applied EdgeR to identify differential chromatin interactions at 50-kilobase (kb) resolution[55]. We found that chromatin interactions linking the E34 subTAD with the Igκ RR and a subTAD located immediately upstream were significantly weakened in pre-B cells derived from E34Δ-*Rag1*$^{-/-}$.hIgM mice (Fig. 3c). Additionally, we found that the E34 subTAD also showed reduced internal interaction frequencies (Fig. 3c). Third, we used FIRE (Frequently Interacting Regions) scores to compare local chromatin interactions across the Igk locus[56]. We found that a genomic region in the vicinity of the E34 enhancer showed strikingly different FIRE scores for E34Δ-*Rag1*$^{-/-}$. hIgM pre-B cells versus WT-*Rag1*$^{-/-}$.hIgM pre-B cells (Fig. 3c). Of note, FitHiC2 analysis also revealed significant interactions involving CTCF binding sites, confirming the boundary element of the E34 subTAD in WT-*Rag1*$^{-/-}$.hIgM pre-B cells (Fig. 3b, brown highlight). The analysis also revealed shifting of a boundary element segregating the E34 subTAD from flanking genomic regions in E34Δ-*Rag1*$^{-/-}$.hIgM pre-B cells (Fig. 3b, green highlight). To determine how changes in subTAD boundaries relate to rearrangement, we calculated V_κ-J_κ rearrangement frequencies for V_κ genes located across the E34 subTAD versus subTADs located upstream. We found a strong correlation between E34-instructed V_κ-J_κ rearrangement frequencies and positioning within or outside the E34 subTAD (Extended Data Fig. 4g). Collectively, these data indicate that the E34 enhancer instructs remote genomic interactions involving the E34 subTAD and the Igκ RR.

E34 instructs chromatin interactions across the Igk locus

The chromatin interaction analysis (EdgeR) indicated that interactions towards the E34 subTAD were significantly reduced in E34Δ-*Rag1*$^{-/-}$. hIgM pre-B cells. A HiC contact matrix at 50-kb resolution confirmed that chromatin interactions involving the E34 subTAD and V_κ subTADs dispersed across the rest of the Igk locus were substantially depleted in E34Δ-*Rag1*$^{-/-}$.hIgM pre-B cells (Fig. 4a, black rectangle). To determine in greater detail how the E34 enhancer orchestrates remote chromatin interactions across the Igk locus, we normalized HiC data using the Knight–Ruiz (KR) algorithm, to remove systematic biases, including DNA fragment length, GC content and DNA sequence mappability, to generate virtual 4C plots using the E34 enhancer as a viewpoint[57]. We found that chromatin interactions involving the E34 enhancer region and genomic regions that span most of the V_κ region were depleted in E34Δ-*Rag1*$^{-/-}$.hIgM pre-B cells (Fig. 4b; E34 viewpoint). Likewise, chromatin interactions involving the E34 enhancer and the Igκ RR were reduced in E34Δ-*Rag1*$^{-/-}$.hIgM pre-B cells (Fig. 4b; E34 viewpoint). As expected, using the Igκ RR as a viewpoint, we observed a decline in contact frequencies across the E34 subTAD in E34Δ-*Rag1*$^{-/-}$.hIgM pre-B cells (Fig. 4b). We found, using an anchor in the V_κ subTAD located immediately upstream of the E34 subTAD, that in E34Δ-*Rag1*$^{-/-}$.hIgM pre-B cells chromatin interactions were depleted for a genomic region that spanned the E34 subTAD, consistent with a decline in IS (increased insulation) (Figs. 4b and 2d). Finally, we found that the relative decline in contact frequencies for paired E34 subTAD-Igκ RR chromatin interactions correlated well with changes in V_κ-J_κ rearrangement frequencies (Fig. 4c). Zooming onto significant interaction frequencies depleted in E34Δ-*Rag1*$^{-/-}$.hIgM pre-B

cells, revealed by FitHiC2, indicated that these interactions involve the CER element (Extended Data Fig. 5a, blue rectangle). Chromatin interactions emanating from the iE_κ and the J_κ elements were depleted as well in E34Δ-*Rag1*$^{-/-}$.hIgM pre-B cells (Extended Data Fig. 5a, black rectangle). To determine how E34 instructs interactions involving the iE_κ enhancer and the CER element, we generated virtual 4C plots from KR-normalized data at 10-kb resolution (Extended Data Fig. 5b). We found that chromatin interactions involving the iE_κ and the CER element were differentially affected in E34Δ-*Rag1*$^{-/-}$.hIgM versus WT-*Rag1*$^{-/-}$.hIgM mice pre-B cells. In sum, these data indicate that the E34 enhancer enriches for chromatin interactions between the E34 subTAD with structural (V_κ subTADs and CER) and coding/regulatory (IgκRR) elements.

E34 repositions the E34 subTAD away from heterochromatin

To determine whether the E34 enhancer modulates E34 subTAD euchromatic versus heterochromatic compartmentalization, we performed a principal component (PC) analysis across the Igk locus[58]. We found reduced PC1 scores across the E34 subTAD in pre-B cells derived from E34Δ-*Rag1*$^{-/-}$.hIgM mice when compared with pre-B cells isolated from WT-*Rag1*$^{-/-}$.hIgM mice (Fig. 4d). The change in PC1 values across the E34 subTAD raised the possibility that loss of the E34 enhancer instructed interactions with genomic regions positioned in a segregated environment. As a first approach to test this possibility, we quantified the degree of compartment segregation across the Igk locus and flanking regions by plotting contact frequencies as saddle and violin plots[17]. We found a decline in compartmental segregation scores in E34Δ-*Rag1*$^{-/-}$. hIgM pre-B cells when compared with WT-*Rag1*$^{-/-}$.hIgM pre-B cells (Fig. 4e,f). To examine whether the E34 enhancer interferes with the repositioning of the E34 subTAD with putative heterochromatic regions adjacent to the Igk locus, we generated Pearson correlation matrices. We found that in E34Δ-*Rag1*$^{-/-}$.hIgM pre-B cells, the E34 subTAD was associated with a heterochromatic region located upstream of the Igk locus, while the association with the remainder of the V_κ region was depleted (Fig. 4g, black and blue rectangles). In sum, these data indicate that the E34 enhancer segregates the E34 subTAD away from genomic regions associated with heterochromatin.

E34 instructs chromatin remodeling across the E34 subTAD

The aforementioned data indicate that E34 instructs the nuclear repositioning of the E34 subTAD. To determine whether the E34-dictated relocation of the E34 subTAD away from a genomic region enriched for heterochromatin instructs changes in chromatin accessibility, we performed an assay for transposase-accessible chromatin using sequencing (ATAC-seq) analysis. We found that chromatin accessibility across the entire E34 subTAD was virtually abolished in E34Δ-*Rag1*$^{-/-}$.hIgM pre-B cells (Fig. 5a, red highlight, and Fig. 5c). To determine whether and how E34-instructed alterations in chromatin accessibility relate to changes in the deposition of epigenetic marks, we examined for changes in H3K27Ac and H3K4me1 abundance (Fig. 5b). As expected, we found that H3K27Ac occupancy at the E34 enhancer was abolished in E34Δ-*Rag1*$^{-/-}$.hIgM pre-B cells (Figs. 5b and 6a, green arrows). H3K4me1 abundance also declined across the entire E34 subTAD (Fig. 5b, beige highlight, and Figs. 5d and 6a). Likewise, H3K27me3 abundance within the E34 subTAD declined upon excision of the E34 enhancer (Fig. 5b, purple highlight, and Fig. 5f). Conversely,

H3K9me3 abundance was modestly increased (Fig. 5b, yellow highlight, and Fig. 5g). In sum, these data indicate that the E34 enhancer instructs chromatin accessibility as well as H3K27Ac and H3K4me1 abundance across the E34 subTAD.

E34 enhancer instructs transcription and CTCF occupancy

CTCF occupancy also was reduced across the E34 subTAD in pre-B cells derived from E34Δ-*Rag1*$^{-/-}$.hIgM mice (Fig. 5b, green highlight, and Fig. 6a). Zooming-in to the E34 subTAD 5′ region, where the impact of the E34 excision ceased, revealed a CTCF binding site located between *Igkv5–43* and *Igkv12–42* (Extended Data Fig. 6a, red rectangle). These findings are consistent with this CTCF site functioning as a 5′ boundary element of the E34 subTAD, validating the aforementioned analysis of boundary elements that span the Igk locus in E34Δ-*Rag1*$^{-/-}$.hIgM cells (Fig. 2d). Noncoding transcription throughout the E34 subTAD was also ablated in E34Δ-*Rag1*$^{-/-}$.hIgM pre-B cells (Fig. 5b, blue arrows, Figs. 5e and 6a, and Extended Data Fig. 6b–d). The aforementioned analysis of chromatin interactions involving the IgκRR and the E34 subTAD showed that this subset of interactions was associated with CTCF occupancy and the deposition of enhancer-associated epigenetic marks (Fig. 3b). Upon closer inspection, we found that depletion of these interactions correlated with a reduction in CTCF occupancy (red arrows) and enhancer-associated epigenetic marks (green arrows) in E34Δ-*Rag1*$^{-/-}$.hIgM pre-B cells (Fig. 6a, blue highlights). Several CTCF-bound sites affected were in convergent orientation as compared with DNA sequences associated with CTCF-bound sites in the CER element, including a prominent CTCF binding site nearby the *Igkv8–28* element (Fig. 6a–c). Taken together, these data indicate that the E34 enhancer promotes CTCF occupancy, noncoding transcription to facilitate interactions with CTCF-bound sites in the CER.

E34 instructs chromatin accessibility across the RSSs

Previous studies demonstrated that chromatin accessibility and H3K4me1 binding at the RSSs are closely associated with V-gene rearrangement fitness[40,41,59–62]. To evaluate how changes in the level of these epigenetic signatures at the RSSs affected V_κ gene rearrangement, we re-examined ATAC-seq and H3K4me1 reads. We found that reduced chromatin accessibility and H3K4me1 abundance at genomic regions spanning the V_κ gene RSSs was confined to the E34 subTAD in E34Δ-*Rag1*$^{-/-}$.hIgM pre-B cells (Fig. 6d,e). The differential enrichment analysis also revealed that the reduction in V_κ rearrangement correlated with a decrease in chromatin accessibility and H3K4me1 abundance at the RSSs (Fig. 6f,g). The reduction in chromatin accessibility and H3K4me1 abundance was particularly prominent for the *Igkv7–33* gene (Fig. 6h). In sum, these data indicate that the E34 enhancer controls chromatin accessibility at RSSs of nearby-located V_κ genes.

E34 repositions nearby V_κ genes

Recruitment of the antigen receptor loci to the pericentromeric heterochromatin is a hallmark of V(D)J recombination inactivation[38]. While pericentromeric heterochromatin is defined, at least in part, by the deposition of H3K9me3, facultative heterochromatin is enriched for H3K27me3. The data described above indicate that the E34 enhancer instructs the repositioning of the E34 subTAD from a heterochromatic environment to a recombination-permissive compartment. To determine whether the E34 subTAD is located

in constitutive versus facultative heterochromatin in E34Δ-*Rag1*$^{-/-}$.hIgM pre-B cells, we combined HiC Pearson correlation matrices with enrichment for H3K9me3 and H3K27me3. We found that in the absence of the E34 enhancer, the E34 subTAD was markedly associated with a genomic region that was enriched for the deposition of H3K9me3 (Fig. 7a, black dashed rectangles). Using KR-normalized HiC data, we found that chromatin interactions of the E34 subTAD in E34Δ-*Rag1*$^{-/-}$.hIgM pre-B cells extended beyond the Igk locus and correlated with negative PC1 scores and the deposition of H3K9me3 but not with H3K27me3 (Fig. 7b–f). Rather, enrichment for H3K27me3 appeared to be inversely correlated (Fig. 7d and Extended Data Fig. 6e). Taken together, these data indicate that the E34 enhancer orchestrates the nuclear repositioning of the E34 subTAD away from the constitutive pericentromeric heterochromatin compartment to a recombination-permissive environment.

E34 instructs a distinct anti-bacterial antibody repertoire

It is well documented that natural EO6/T15 antibodies directed against *S. pneumoniae* in the serum of naïve mice confer strong protection against challenge with the bacterium[43,45]. Since our observations indicated that E34 promotes V_κ gene rearrangement associated with EO6/T15 antibodies, we examined serum derived from WT and E34Δ mice for the presence of anti-phosphorylcholine and EO6/T15 antibodies. We found that anti-phosphorylcholine and EO6/T15 antibody titers were reduced in E34Δ mice (Fig. 8a,b). To test whether the decrease in antibody concentration impacted survival, serum derived from WT or E34Δ mice was mixed with *S. pneumoniae* and injected intraperitoneally in *Rag1*$^{-/-}$ mice. We found that the entire mouse cohort challenged with the bacterium and serum isolated from E34Δ mice died by day 4, while 31% of mice survived through day 7 when the serum was derived from WT mice (Fig. 8c,d). To determine the kinetics of the production of EO6/T15 antibody, we inoculated heat-killed *S. pneumoniae* intraperitoneally in WT and E34Δ mice. We found that the EO6/T15 antibody titers elicited were significantly higher in WT mice when compared with E34Δ mice (Fig. 8e,f). Next, we challenged mice intravenously with *S. pneumoniae*, finding that E34Δ mice exhibited significantly higher mortality than WT mice (Fig. 8g,h).

As a first approach to determine whether E34-instructed V_κ-J_κ rearrangement specifically affected the pathogenesis of *S. pneumoniae*, we challenged WT and E34Δ mice with MRSA, which lacks phosphorylcholine in the cell wall (Fig. 8g,i). We found that WT and E34Δ mice showed similar mortality rates for either high or low doses when infected intravenously with MRSA (Fig. 8i). Previous studies demonstrated that natural and induced IgM antibody responses provide protection against influenza virus infection[63]. To determine whether E34-instructed antibody repertoires warrant resistance against influenza infection, we challenged WT and E34Δ mice with influenza virus. To this end, WT and E34Δ mice were intranasally infected with influenza. We found that WT and E34Δ mice showed similar mortality rates when infected with influenza virus (Fig. 8j). Collectively, these observations indicate that the E34 enhancer instructs the generation of antibodies that confer protection against lethal *S. pneumoniae* infection but not lethal MRSA or influenza infections.

Discussion

The majority of antigen receptor loci are associated with immense numbers of V regions scattered across vast genomic distances, raising the question of how V regions encounter D or J elements with distinct probabilities independent of genomic separation. Here, we reveal in mechanistic terms how enhancers instruct V_κ-J_κ rearrangement. Specifically, we identified an enhancer, termed E34, in the Igk locus that repositions a V_κ subTAD away from a recombination-silent to a recombination-permissive neighborhood. How does the E34 enhancer perform this daunting task? We show that in pre-B cells, the transcription factors E2A, EBF1 and PAX5 are sequestered at the E34 enhancer[32,34,46,47,64]. Upon binding, these factors act collaboratively to deposit activating histone marks, including H3K27Ac and H3K4me1, across the E34 subTAD[34,48,65–68]. We propose that the deposition of transcriptionally activating histone marks physically pulls the E34 subTAD into a segregated compartment that harbors J_κ gene segments and other V_κ elements, marked by equivalently activating histone marks.

In addition to the deposition of epigenetic marks, we found that the repositioning of V_κ genes into a segregated compartment is closely associated with E34-dependent noncoding transcription. How is noncoding transcription linked to changes in compartmentalization? Previous studies have demonstrated that noncoding transcription across the T-cell receptor J_α elements instructs the removal of repressive epigenetic marks and promotes deposition of transcriptionally activating histone marks as well as chromatin accessibility across the RSSs[69]. We suggest that the induction of E34-dependent transcription across the E34 subTAD acts similarly across the E34 subTAD. Likewise, we suggest that noncoding transcription instructed by the iE_κ enhancer promotes the deposition of transcriptionally activating marks across the J_κ region[70]. We propose that when transcriptionally repressive epigenetic information is replaced with the deposition of transcriptionally activating histone marks, V_κ and J_κ compartmental domains physically merge into a shared compartmental domain, a process that is likely driven by phase separation[71]. We note, however, that noncoding transcription might also act in a second pathway to instruct local chromatin folding across the E34 subTAD. Specifically, we favor a model in which E34-instructed activation of noncoding transcription across the E34 subTAD increases CTCF occupancy at weak-affinity binding sites[72]. Alternatively, noncoding transcription may promote DNA demethylation at CTCF binding sites to facilitate occupancy[73,74]. Thus, the cardinal conclusion of these observations is that the merging of V_κ genes with J_κ elements in a segregated nuclear structure is instructed by one-dimensional epigenetic information imposed by transcription factors and CTCF-dependent chromatin folding.

Finally, as aforementioned, the E34 enhancer is located within close genomic proximity of a V_κ gene encoding for the light chain associated with the EO6/T15 antibody idiotype. The EO6/T15 antibody is of particular clinical interest since it targets phosphorylcholine expressed on the *S. pneumoniae* cell wall[42–45]. Phosphorylcholine is found on the surface of a variety of pathogens that colonize the upper respiratory tract, including members of the genera *Streptococcus*, *Haemophilus* and *Neisseria*[75]. By altering the chromatin domain topology in the Igk locus, we negatively impacted the EO6/T15 V_κ rearrangement frequency. As a consequence, the EO6/T15 steady-state and stimulation-

mediated responses were hampered, and, as predicted, depletion of EO6/T15 and EO6/T15-expressing B cells caused significantly increased mortality upon *S. pneumoniae* challenge. EO6/T15 antibodies belong to a class of antibodies often referred to as natural antibodies which are essential for early immune responses against pathogens[76]. These are mainly produced in the absence of prior antigenic exposure by B1a B cells, tend to be of the IgM isotype and target pathogen-associated epitopes. Natural antibodies are also involved in tissue homeostasis; for example, EO6/T15 may protect the host by binding oxidized phospholipids[77]. Produced in inflammatory tissues, including atherosclerotic lesions, oxidized phospholipids are proinflammatory and promote the development of atherosclerosis and nonalcoholic steatohepatitis[78]. Numerous studies have indicated the potential of EO6/T15 antibodies to protect against atherosclerosis and nonalcoholic steatohepatitis by recognizing phosphorylcholine in oxidized phospholipids[79,80–82]. In future work, it will be important to determine whether E34Δ mice show increased susceptibility to cardiovascular disease or nonalcoholic steatohepatitis.

Recently, it was shown that precursor B cell frequencies play a crucial role in developing effective immune responses[83–86]. Specifically, the number of precursor B cells of the VRC01-class, which have the potential to generate broadly neutralizing antibodies against the HIV envelope glycoprotein, is critical for competition in the germinal center reaction and the generation of memory B cells after immunization[83,84]. The significance of precursor frequency has also been observed in other systems, including in mice expressing the human IGHV1–69 gene, which generates broadly neutralizing anti-influenza B cell responses[85,86]. Furthermore, disruption of enhancer function has been increasingly associated with disease, specifically involving genetic variants in transcription factor binding sites[87]. Polymorphisms also can affect the recombination frequencies of specific V genes and are correlated with disease[88–90]. It seems likely that polymorphisms associated with antigen receptor loci enhancers affect V-gene rearrangement frequencies in human B cells, with implications for human disease and vaccine development.

In conclusion, our studies indicate that the merging of V_κ genes with J_κ elements is instructed by one-dimensional epigenetic information imposed by enhancers across V_κ and J_κ genomic regions. We propose that the deposition of specific epigenetic marks physically pulls the E34 subTAD into a segregated compartment containing J_κ elements and other V_κ genes dispersed across the Igk locus, likewise marked by equivalent active histone marks. Finally, the data also reveal how enhancers act to generate distinct antibody repertoires that provide protection against lethal bacterial infection.

Methods

Mice

All mice were maintained in our breeding facility in accordance with protocols approved by Institutional Animal Care and Use Committee of the University of California San Diego (La Jolla, CA). Both male and female mice were used, ages 6–12 weeks. All mice used were in a C57BL/6 background.

Flow cytometry and cell sorting

Isolated cell suspensions from organs or tissue cavities were counted and washed with 5 ml of Dulbecco's phosphate buffered saline (D-PBS). Cells were resuspended at a final concentration of 10^5 cells per µl in a minimal volume of 50 µl in a solution of FACS buffer containing 1/100 dilution of purified rat anti-mouse CD16/CD32, Mouse BD Fc Block (cat. no. 553142, Fisher). Cell were stained with antibodies (Supplementary Table 2) for each population identification (Extended Data Fig. 2a–c) in a concentration of 1/200 for 25 min. Cells were washed with 3 ml of D-PBS and resuspended in 500–800 µl for flow cytometry or 1–3 ml for FACS. Data were analyzed using FlowJo v.10.7.

Generation of the E34Δ mice

We used CRISPR–Cas9 to make germline mutations in mice zygotes. We used small guide RNAs (sgRNAs), sgRNA1 (TGGCAAGCTGCCTTTAAAGA) and sgRNA2 (5′-ACCTTAACTCTGAGAGATAA), from Integrated DNA Technologies, Alt-R CRISPR–Cas9 CRISPR RNA (crRNA) and Alt-R CRISPR–Cas9 transactivating crRNA (tracrRNA). We mixed 1 µl of 100 µM of each Alt-R CRISPR–Cas9 crRNA with 1 µl of 100 µM Alt-R CRISPR–Cas9 tracrRNA with 98 µl of Nuclease-free Duplex buffer (Integrated DNA Technologies). The mix was heated at 95 °C for 5 min and allowed to cool at 20 °C. Cas9 protein (NEB no. M0646T), crRNA and tracrRNA were added to a final concentration of 0.6 µM each in a volume of 30 µl of TE buffer. This mix was incubated for 5 min at 20 °C. The mix was centrifuged and the supernatant (25 µl) was transferred to a new tube. The sample was kept on ice until the pronuclear injection. Injection of guide RNAs and implantation were carried out at the University of California San Diego Transgenic Core Facility. C57BL/6NHsd female mice and ICR mouse strains were used as embryo donors and foster mothers, respectively. C57Bl/6NHsd females (4–5 weeks old) were super-ovulated with pregnant mare serum gonadotropin (PMSG) and human chorionic gonadotropin (HCG), and mated to C57BL/6NHsd males. One-cell stage fertilized embryos were collected from oviducts the next day. CRISPR mixture was injected into the pronucleus of fertilized eggs. All injected embryos were then implanted in the oviduct of pseudo-pregnant ICR females.

RNA and DNA isolation

RNA and genomic DNA (gDNA) samples were prepared from 2×10^5 to 2×10^6 pro-B, pre-B, B1a and B1b cells using QIAshredder (cat. no. 79654, Qiagen). Gating schemes for each B cell population are shown in Extended Data Fig. 2a–c. RNA was isolated using an RNeasy Plus Mini Kit (cat. no. 74134, Qiagen). DNA was isolated ($1–3 \times 10^6$ cells) using a DNeasy Blood and Tissue Kit (cat. no. 69504, Qiagen). DNA and RNA samples were processed according to instructions provided by the manufacturers.

RNA-seq

RNA-sequencing (RNA-seq) libraries were generated using the Illumina Ribo-Zero Plus rRNA Depletion Kit with IDT for Illumina RNA UD Indexes (Illumina). Samples were processed following manufacturer instructions. Resulting libraries were multiplexed and sequenced with 100-base pair paired-end reads (PE100) to a depth of approximately 25

million reads per sample on an Illumina NovaSeq 6000. Samples were de-multiplexed using bcl2fastq v.2.20 Conversion Software (Illumina).

Library preparation for V_κ repertoire sequencing

Complementary DNA was prepared using QuantiTect Reverse Transcription kit from RNA isolated from 2×10^5 to 2×10^6 cells according to manufacturer instructions. cDNA libraries were quantified by quantitative PCR for total rearrangement using a panspecific V_κ gene primer ($V_\kappa$all 5′-GGCTGCAGSTTCAGTGGCAGTGGRTCWGGR AC-3′)[70] and a primer in the constant region (C_κ 5′-TGGTGGGAAGATGGATACAGTTGGTG-3′). For gDNA amplification, primers downstream of J_κ1 (5′-GGATTCTACTTACGTTTGATTTCCA-3′) and J_κ5 (5′-GAAAAGTGTACTTACGTTTCAGCT-3′) were used instead of Ck. Next, samples were amplified in eight independent PCR reactions using Q5 High-Fidelity 2X Master Mix (M0492S, NEB), to avoid PCR biases, until two cycles before the calculated threshold cycle (C_t) value from the first quantification. These eight reactions were pooled and cleaned using NucleoSpin Gel and PCR Clean-up kit (REF 740609.50, Macherey-Nagel). The V_κ PCR library was prepared for Illumina sequencing with KAPA HyperPrep Kit (KK8502) using KAPA Unique Dual-Indexed Adapters (KK8727).

V_κ repertoire analysis

MiXCR software was used for analysis of V_κ gene rearrangement[91]. Data from all clonotypes and all the J_κ gene recombination events for each V_κ gene were added and reported as a percentage of the total rearrangement.

The following command lines were used:

- ./mixcr align --species mmu <filenameR1>.fastq.gz <filenameR2>.fastq.gz <output_filename1>.vdjca
- ./mixcr assemble -a <output_filename1>.vdjca <output_filename1>.cln
- ./mixcr exportClones <output_filename1>.clna <output_filename1>.txt

HiC

WT-*Rag1*$^{-/-}$.hIgM and E34Δ-*Rag1*$^{-/-}$.hIgM CD19$^+$ cells were isolated from bone marrow by column separation using CD19 microbeads (cat. no. 130–121-301, Miltenyl Biotec). Two biological replicates from a pool of 2–4 mice each were used to prepare the HiC library. Ten million CD19$^+$ cells were used for processing. Arima-HiC$^+$ kit (cat. no. A101020) was used to prepare the HiC libraries according to instructions provided by manufacturers.

HiC data preprocessing

We used our in-house HiC data analysis pipeline to preprocess the HiC data (https://github.com/ren-lab/hic-pipeline), as described in our previous studies[56,92,93]. Briefly, we mapped each single-end read from the fastq files to the reference genome mm9, retained uniquely mapped reads and removed PCR duplicates. Next, we used the juicer software[94] (https://github.com/aidenlab/juicer) to convert mapped reads into the .hic files. Finally, we

generated 50-kb-bin-resolution HiC raw contact matrices from the .hic files for further analysis.

HiC reproducibility

First, we calculated the Pearson correlation coefficients between the raw counts of two biological replicates at the same genomic distance. We found that for 500-kb genomic distances, the Pearson correlation coefficient was 0.9263 and 0.9008 for WT-*Rag1*$^{-/-}$.hIgM and E34Δ-*Rag1*$^{-/-}$.hIgM pre-B cells, respectively. We further applied HiCrep to calculate the stratum-adjusted correlation coefficient, with the smoothing parameter $h = 5$ and maximal genomic distance of 2 megabases (Mb) (ref. [95]). We found that the stratum-adjusted correlation coefficient was 0.9900 and 0.9631 for WT-*Rag1*$^{-/-}$. hIgM and E34Δ-*Rag1*$^{-/-}$.hIgM pre-B cells, respectively. This was followed by merging two biological replicates for each cell type for further analysis.

A/B compartmental domain analysis

We used the 50-kb-bin-resolution HiC raw contact matrices as the input and applied the PC analysis approach to generate PC1 score for chromosome 6 (ref. [58]). We assigned PCs such that 50-kb bins with positive PC1 have higher GC content than 50-kb bins with negative PC1, where the GC content is defined as in ref. [6] (http://enhancer.sdsc.edu/yunjiang/resources/genomic_features/). We defined 50-kb bins with positive PC1 values as being positioned in the A compartment versus 50-kb bins with negative PC1 values being localized in the B compartment.

TAD analysis

We applied the IS method to identify the boundary regions of the TAD[53]. Specifically, we first used the KRnorm method to normalize the 50-kb-bin-resolution HiC raw contact matrices[14]. Next, we defined the local region for each 50-kb bin as the upstream 250 kb and the downstream 250 kb (0.5 Mb in total). Then, we calculated the summation of KRnorm-normalized HiC contact frequency between the upstream 250-kb region and the downstream 250-kb region, and the summation of KRnorm-normalized HiC contact frequency for all bin pairs within the 0.5-Mb region, and defined their ratio as the IS. Finally, we defined a 50-kb bin as the TAD boundary if it showed the lowest IS within a 0.5-Mb genomic region.

FIRE analysis

We applied the HiCNormCis method to normalize the total number of local (<200 kb) intra-chromosomal interactions for each 50-kb bin. We further converted HiCNormCis outputs into *Z*-scores and defined 50-kb bins unusually high in local interactions (that is, *Z*-score above 1.96) as FIRE bins.

ATAC-seq

Sorted pre-B cells were frozen and keep at −80 °C in RPMI medium supplemented with 10% FBS, 2 mM L-glutamine, 1% penicillin/streptomycin, 0.05 mM β-mercaptoethanol and 5% dimethylsulfoxide. Permeabilized nuclei were obtained by resuspending cells in 250 μl of Nuclear Permeabilization Buffer (0.2% IGEPAL-CA630 (I8896, Sigma), 1 mM

dithiothreitol (D9779, Sigma), Protease inhibitor (05056489001, Roche), 5% BSA (A7906, Sigma) in PBS (10010–23, Thermo Fisher Scientific)) followed by incubation for 10 min on a rotator at 4 °C. Nuclei were pelleted by centrifugation for 5 min at 500*g* at 4 °C. The pellet was resuspended in 25 μl of ice-cold Tagmentation Buffer (33 mM Tris-acetate (pH 7.8) (BP-152, Thermo Fisher Scientific), 66 μM potassium acetate (P5708, Sigma), 11 μM magnesium acetate (M2545, Sigma), 16% DMF (DX1730, EMD Millipore) in H_2O (46000-CM, Corning)). An aliquot was then taken and counted by hemocytometer to determine nuclei concentration. Approximately 50,000 nuclei were resuspended in 20 μl of ice-cold Tagmentation Buffer, and incubated with 1 μl of Tagmentation Enzyme (FC-121–1030; Illumina) at 37 °C for 30 min. Tagmented DNA was purified using MinElute PCR purification kit (28004, Qiagen). Libraries were amplified using NEBNext High-Fidelity 2X PCR Master Mix (M0541, NEB) with primer extension at 72 °C for 5 min, denaturation at 98 °C for 30 s, followed by 8 cycles of denaturation at 98 °C for 10 s, annealing at 63 °C for 30 s and extension at 72 °C for 60 s. Amplified libraries were then purified using MinElute PCR purification kit (28004, Qiagen), and two size-selection steps were performed using SPRIselect beads (B23317, Beckman Coulter) at 0.55× and 1.5× bead-to-sample volume ratios, respectively.

CUT&RUN

The protocol used for CUT&RUN was from ref. [96], with some modifications as follows: 33.3 μl of Concanavalin A beads (Bangs Laboratories, cat. no. BP531) were used per 1 × 10^6 cells; 1–3 × 10^6 cells were used per sample; and incubation of nuclei-bound beads with antibody was done overnight at 4 °C on a rotating platform. All antibodies were used at a 1/100 dilution. DNA purification after fragment release was done using NucleoSpin Gel and PCR Clean-up kit (ref. no. 740609.50, Macherey-Nagel). CUT&RUN libraries for Illumina sequencing were prepared with KAPA HyperPrep Kit (KK8502) using KAPA Unique Dual-Indexed Adapters (KK8727). Protein A-MNase (pA-MN) was kindly provided by Dr. Henikoff (Basic Sciences Division, Fred Hutchinson Cancer Research Center, Seattle, Washington, USA). Antibodies used are described in Supplementary Table 2.

ELISA

Wells in an ELISA microplate, Greiner Bio-One (cat. no. 7000101, Fisher scientific), were covered with 50 μl of D-PBS containing anti-mouse T15 V_H and T15 V_L regions of IgM (cat. no. BE0072, BioX Cell) or PC-BSA (cat. no. PC-1011–10, Biosearch Technologies) at a concentration of 5 μg ml^{-1}. Plates were incubated overnight at 4 °C. Solution was removed and wells were washed three times with ELISA wash buffer (0.05% Tween 20 in D-PBS). Wells were blocked with 50–100 ml of blocking buffer (1% BSA in D-PBS) for 30 min. Blocking buffer was removed and wells were washed three times with ELISA wash buffer. Serial dilutions of serum in wash buffer were loaded (50–100 ml) into the wells and were incubated for 2 h at 20 °C. Serum suspensions were removed, and wells were washed three times with ELISA wash buffer. A solution (100 μl) of goat anti-mouse IgM (cat. no. 1021–05, Southern Biotech) at 1/5,000 dilution in D-PBS was added to the wells and incubated for 1 h at 20 °C. Goat anti-mouse IgM solution was removed and wells were washed six times with ELISA wash buffer. TMB substrate (cat. no. 421101, Biolegend) was prepared according to the manufacturer instructions and was added to each well (100 μl).

After 30 min of incubation, 50 µl of stop solution (1 M H_3PO_4) was added to each well on top of the TMB substrate. After 5 min of incubation, the plate was read at 450 nm and 570 nm. Reads at 570 nm (background) were subtracted from those measured using 450 nm to obtain the final optical density.

Serum isolation

Mouse blood was collected by cheek puncture in a 1.5-ml Eppendorf tube. Samples were incubated for 30–60 min at 20 °C to allow coagulation. Samples were centrifuged for 10 min at 1,500*g*. For each sample, supernatant (serum) was collected in an Eppendorf tube and frozen at −20 °C until analysis.

Bacterial and viral cultures and infections

S. pneumoniae strain TIGR4 cultures were grown in Todd-Hewitt broth with 2% yeast extract (THY media). Freshly cultured bacteria from frozen aliquots were grown at 37 °C in 5% CO_2 in THY media. Bacterial cultures, with log phase optical density at 600 nm (OD_{600}) of 0.4, were frozen in 25% glycerol. Bacterial counts were quantified on trypticase soy agar (TSA II) with 10% sheep blood (cat. no. B21162X, Fisher Scientific). For infections, glycerol stocks were thawed and resuspended in cold D-PBS. The suspension was centrifuged at 4,000*g* for 5 min and resuspended in cold D-PBS (same volume as the one used from the glycerol stock). From this suspension, dilutions were made to obtain 50 colony-forming units per 100 ml, based on the original count for the glycerol stock, and were quantified again after each infection. MRSA TCH 1516 was grown in Tryptic Soy Broth to mid-logarithmic phase, washed twice in sterile D-PBS and diluted to obtain the respective inoculums in D-PBS. Mice were briefly anesthetized with isoflurane and injected intravenously with the specified inoculum. Influenza virus strain A/Puerto Rico/8/34 H1N1 was kindly provided by Dr. Alistair Russell (UCSD) at a concentration of 2×10^5 plaque-forming units (PFU) per µl. D-MEM medium was used to dilute the inoculum to a concentration of 1.25 PFU ml^{-1}. Mice were briefly anesthetized with isoflurane and inoculated intranasally with 40 µl of medium containing virus (50 PFU total). Mice were monitored until they fully recovered from anesthesia and monitored for weight loss and mortality for 2 weeks. Mice were humanely euthanized and counted as dead if they lost more than 25% of their initial weight.

Phylogenetic tree

Online resources https://ngphylogeny.fr/ and https://itol.embl.de/ were used to analyze and generate the V_κ gene phylogenetic tree[97–99]. Default tools and parameters were used. Software used by these websites includes: MAFFT Multiple Sequence Alignment Software v.7 (ref. [100]); FastME 2.0: A Comprehensive, Accurate, and Fast Distance-Based Phylogeny Inference Program[101]; BMGE Block Mapping and Gathering with Entropy[102]; and Phylogeny Reconstruction Algorithms[103].

CUT&RUN and ATAC-seq analysis

Fastq files were uploaded to usergalaxy.org[104]. These files were aligned to the mouse genome build mm9 using Bowtie2 (ref. [105]) with the default parameters, except the

minimum and maximum fragment lengths for valid paired-end alignments were set to 10 and 700, respectively, and mate dove tailing was also allowed, and the analysis mode was set to 'Very sensitive local'. Next, Samtools merge was used to combine data from the two biological replicas with default parameters. Then, merged BAM files were converted to bigwig files for visualization in the UCSC Genome Browser using bamCoverage toolset to normalize the samples to reads per kilobase per million (RPKM). Significant peaks were called using MACS2 callpeak for merged BAM files.

RNA-seq analysis

Fastq files were uploaded to usergalaxy.org. RNA STAR Gapped-read mapper for RNA-seq data (Galaxy v.2.7.8a) was run to obtain BAM files with the default parameters[104]. BAM files were converted to bigwig files for visualization in the UCSC Genome Browser.

Statistical analysis

Prism 7 (GraphPad Software) was used to calculate significant differences between samples and the correlation coefficient. The usergalaxy. org website was used for CUT&RUN and ATAC-seq peak calling. DEseq was used to calculate significant differences between samples for CUT&RUN, ATAC-seq and RNA-seq data. A two-sided *Z*-test was used to calculate *P* values for the DI, IS, PC1 score and virtual 4C plots.

Blinding

Data collection and analysis were not performed blind to the conditions of the experiments.

Extended Data

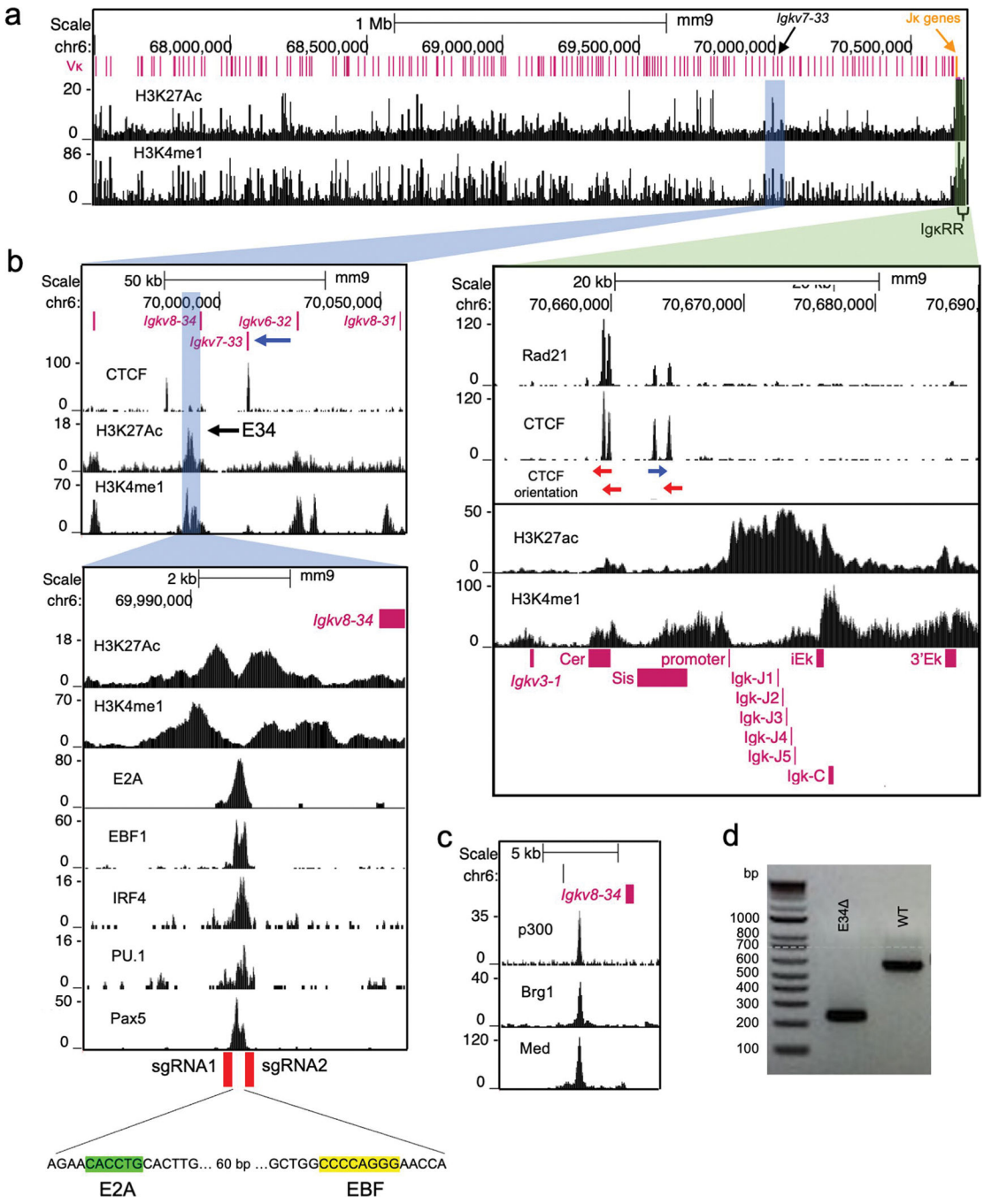

Extended Data Fig. 1 |. Identification of an enhancer located nearby a Vκ gene encoding for the prototypical EO6/T15 antibody idiotype.

a, Genome browser view of the Igκ locus indicating the location of the Vκ gene segments and deposition of H3K27Ac (GSM3103098) and H3K4me1 (GSM2084579) in WT-*Rag1*$^{-/-}$.hIgM pre-B cells. Blue and green highlights indicate a potential enhancer in the vicinity of the *Igkv7–33* gene and the IgκRR, respectively. **b**, Genomic region spanning the *Igkv7–33* gene is shown. CTCF (GSM2973687) occupancy and deposition of H3K27Ac and

H3K4me1 (upper panel) are shown. Lower tracks show enrichment for the deposition of H3K27Ac and H3K4me1. E2A (GSM546523), EBF (GSM1296532), IRF4 (GSM1296534), PU.1 (GSM1296533), and Pax5 (GSM932924) occupancy across the *Igkv7–33* genomic region is indicated. Bottom indicates genomic position of gRNAs used to excise the E34 enhancer. **c**, p300 (GSM987808), Brg1 (GSM1635413), and Mediator (GSM1038263) occupancy across a genomic region spanning the E34 enhancer. **d**, Genotyping of DNA derived from wild-type (WT) cells and cells carrying the E34-targeted deletion is shown. Indicated are representatives from two independent experiments.

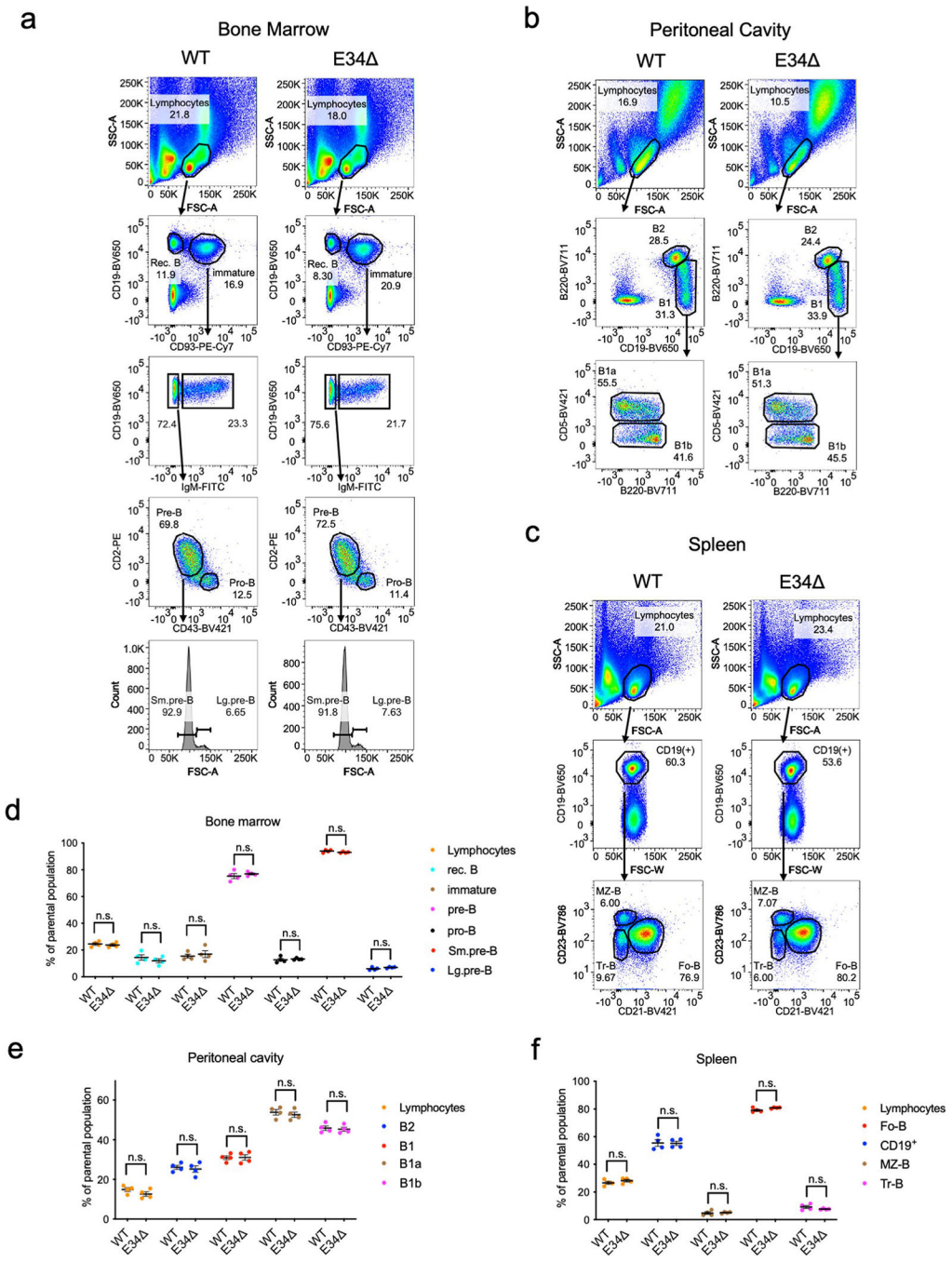

Extended Data Fig. 2 |. Flow cytometric analysis of B cell populations in WT and E34Δ mice.
Gating strategy to identify B cell populations in bone marrow (**a**), peritoneal cavity (**b**), and spleen (**c**) is shown. Forward scatter (FSC) and side scatter (SSC) areas are shown. Quantification of the flow cytometry data for B cell populations derived from bone marrow (**d**), peritoneal cavity (**e**), and spleen (**f**) are indicated. Data was derived from 4 mice for each genotype and expressed as a percentage of the parental population. Data are presented as mean values +/− SEM. Significant differences between populations were assessed using

two-tailed t-test. Small (Sm), Large (Lg), follicular (Fo), marginal zone (MZ), recirculating (rec), and transitional (Tr) B cells are indicated. n.s.=not significant.

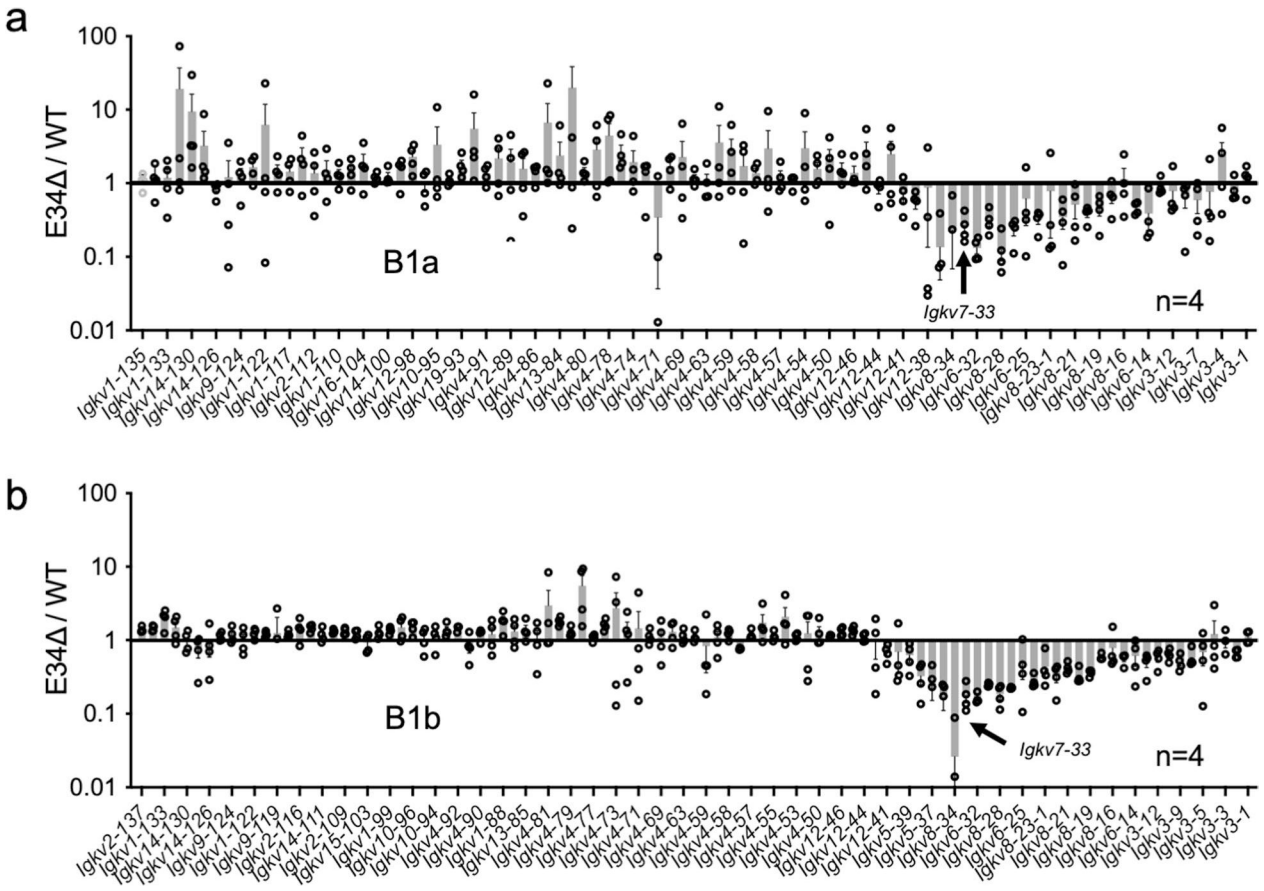

Extended Data Fig. 3 |. Relative Vκ rearrangement frequencies in B1 cell subpopulations derived from WT and E34Δ mice.

Relative Vκ rearrangement frequencies in (**a**) B1a B cells, and (**b**) B1b B cells derived from WT and E34Δ mice are shown. Data was derived from four independent experiments (one mouse per group per genotype) and is expressed as the average of the ratio of E34Δ mice over littermate controls (WT) ± SEM.

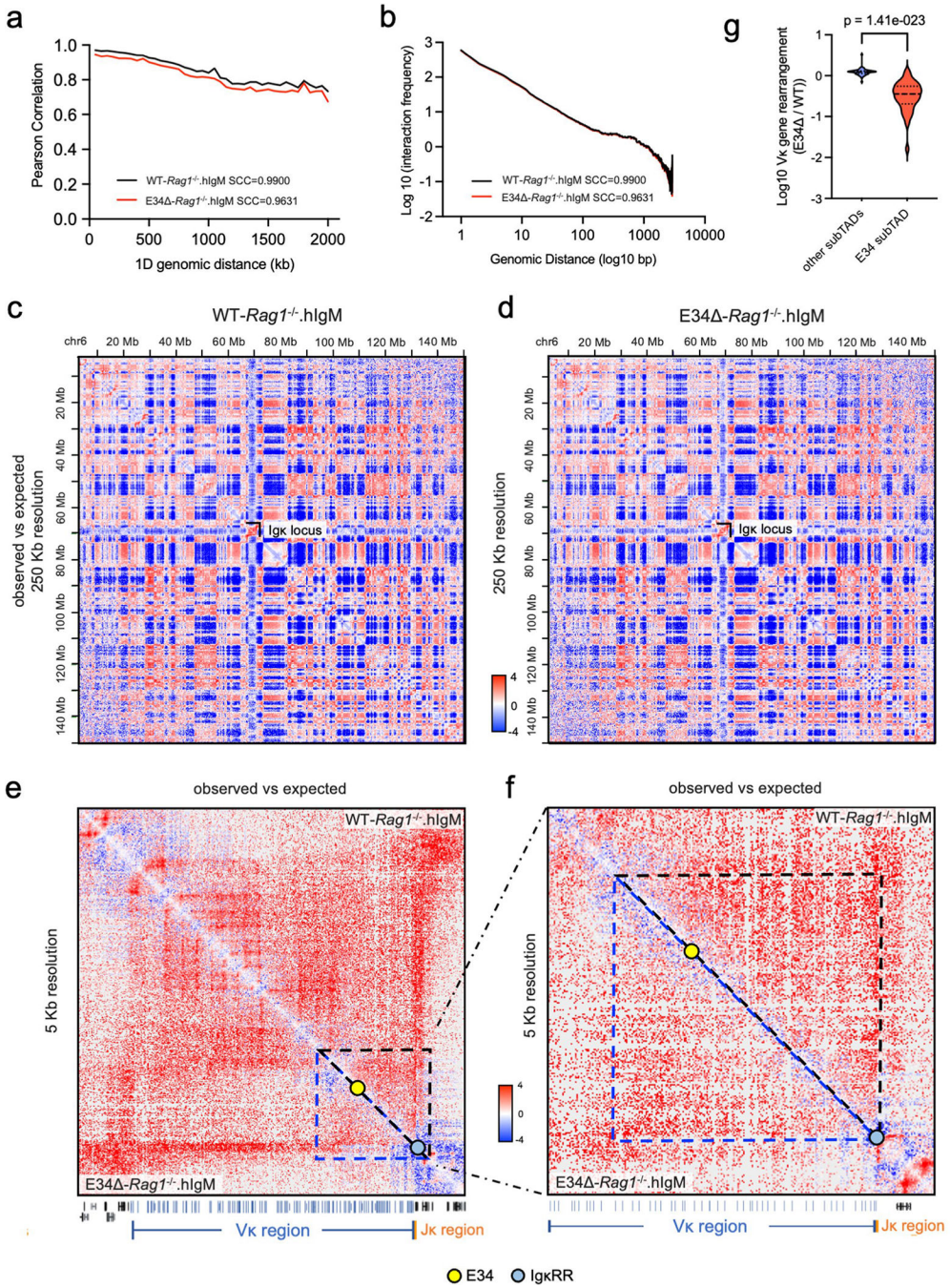

Extended Data Fig. 4 |. HiC, virtual 4 C, Vκ rearrangement and contact frequency correlation analyses.

Pearson correlation assessing the reproducibility of the HiC data for WT-*Rag1*$^{-/-}$.hIgM and E34Δ-*Rag1*$^{-/-}$.hIgM pre-B cells are indicated[95]. Stratum adjusted correlation coefficients (SCC) are shown. **b**, Average contact probability as a function of genomic distance for compiled WT-*Rag1*$^{-/-}$.hIgM and E34Δ-*Rag1*$^{-/-}$.hIgM pre-B cells samples. **c,d**, HiC contact matrices for WT-*Rag1*$^{-/-}$.hIgM (**c**) and E34Δ-*Rag1*$^{-/-}$.hIgM (**d**) pre-B cells across chromosome 6 are shown. The location of the Igk locus is indicated. **e**, HiC contact matrices

for WT-*Rag1*$^{-/-}$.hIgM and E34Δ-*Rag1*$^{-/-}$.hIgM pre-B cell across the Igk locus. **f**, HiC contact matrices for WT-*Rag1*$^{-/-}$.hIgM and E34Δ-*Rag1*$^{-/-}$. hIgM pre-B cells for a genomic region that spans the E34 enhancer. Yellow and blue dots indicate the E34 enhancer and the Igκ RR, respectively. The location of the Vκ (blue), Jκ (orange), and other genes (black) is shown at the bottom. Location of the affected genomic region is indicated by black and blue triangles in WT-*Rag1*$^{-/-}$.hIgM and E34Δ-*Rag1*$^{-/-}$.hIgM pre-B cells. **g**, Significant differences between Vκ gene rearrangement frequencies were computed within and outside of the E34 subTAD assessed using two tailed t-tests.

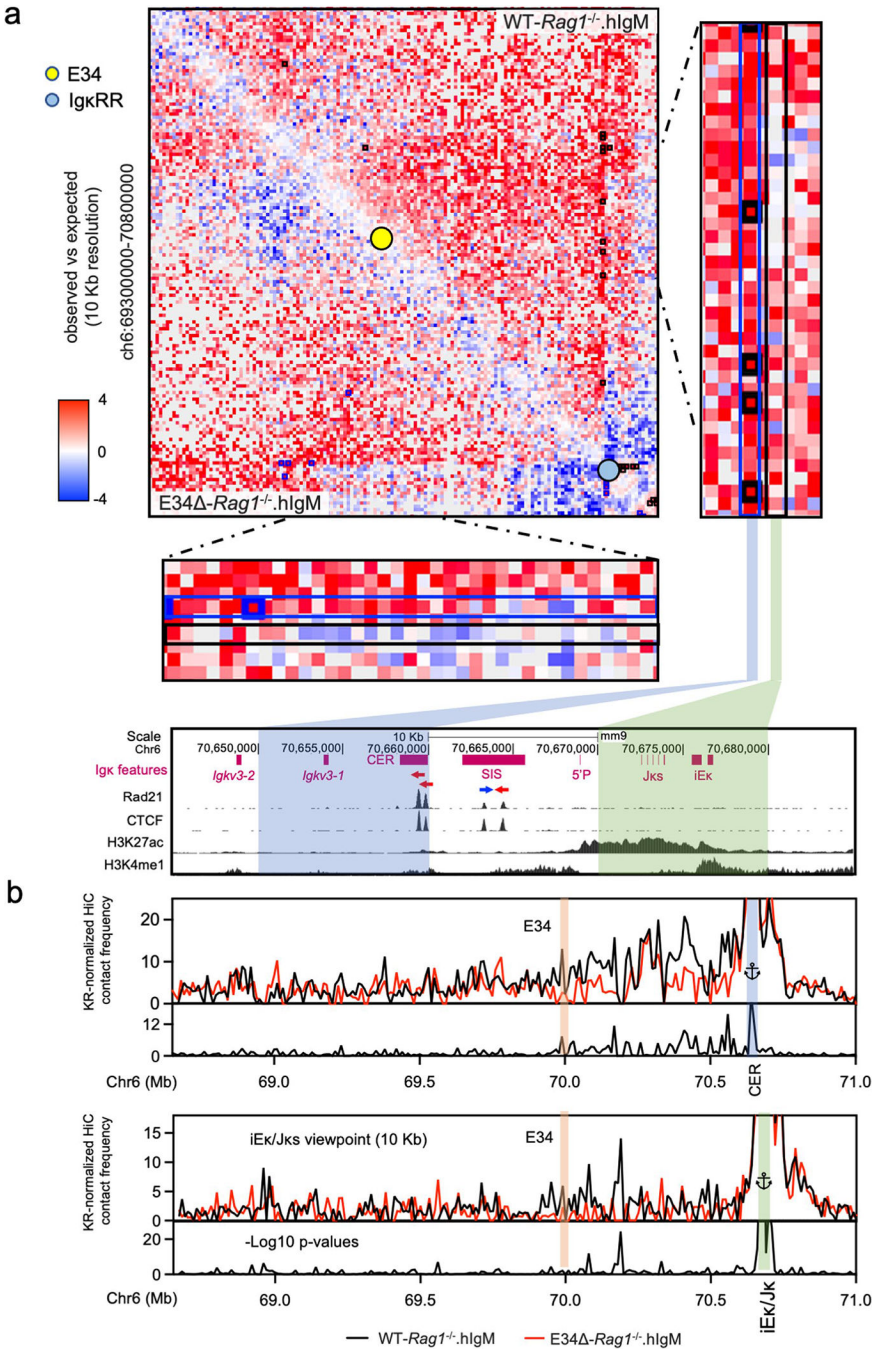

Extended Data Fig. 5 |. Chromatin interactions involving the CER and the iEκ/Jκ elements in WT-*Rag1*$^{-/-}$.hIgM and E34Δ-*Rag1*$^{-/-}$.hIgM pre-B cells.

a, HiC matrix heatmaps showing chromatin interaction frequencies involving a genomic region that spans the E34 subTAD in WT-*Rag1*$^{-/-}$.hIgM and E34Δ-*Rag1*$^{-/-}$. hIgM pre-B cells. Close-up views of HiC matrices heatmap that span a genomic region harboring the CER and the iEκ/Jκ elements are indicated. Blue and black rectangles indicate a 10 kbp genomic region that show interactions involving the CER and iEκ/Jκ elements, respectively. Black and blue squares represent significant chromatin interactions detected by FitHiC2 in WT-*Rag1*$^{-/-}$.hIgM and E34Δ-*Rag1*$^{-/-}$.hIgM pre-B cells, respectively. Bottom tracks indicate

Rad21 and CTCF occupancy as well as the deposition of H3K27Ac and H3K4me1 in a genomic region that spans the CER element and iEκ/Jκ region. **b**, Virtual 4 C plots spanning a 10 kbp genomic region contain the CER and the iEκ/Jκ element in the vicinity of the E34 enhancer in WT-*Rag1*$^{-/-}$.hIgM and E34Δ-*Rag1*$^{-/-}$.hIgM pre-B cells. Significant differences were calculated using a two-sided Z-test. The negative log10 p-values indicating significant differences between WT-*Rag1*$^{-/-}$.hIgM and E34Δ-*Rag1*$^{-/-}$.hIgM cells are shown at the bottom tracks.

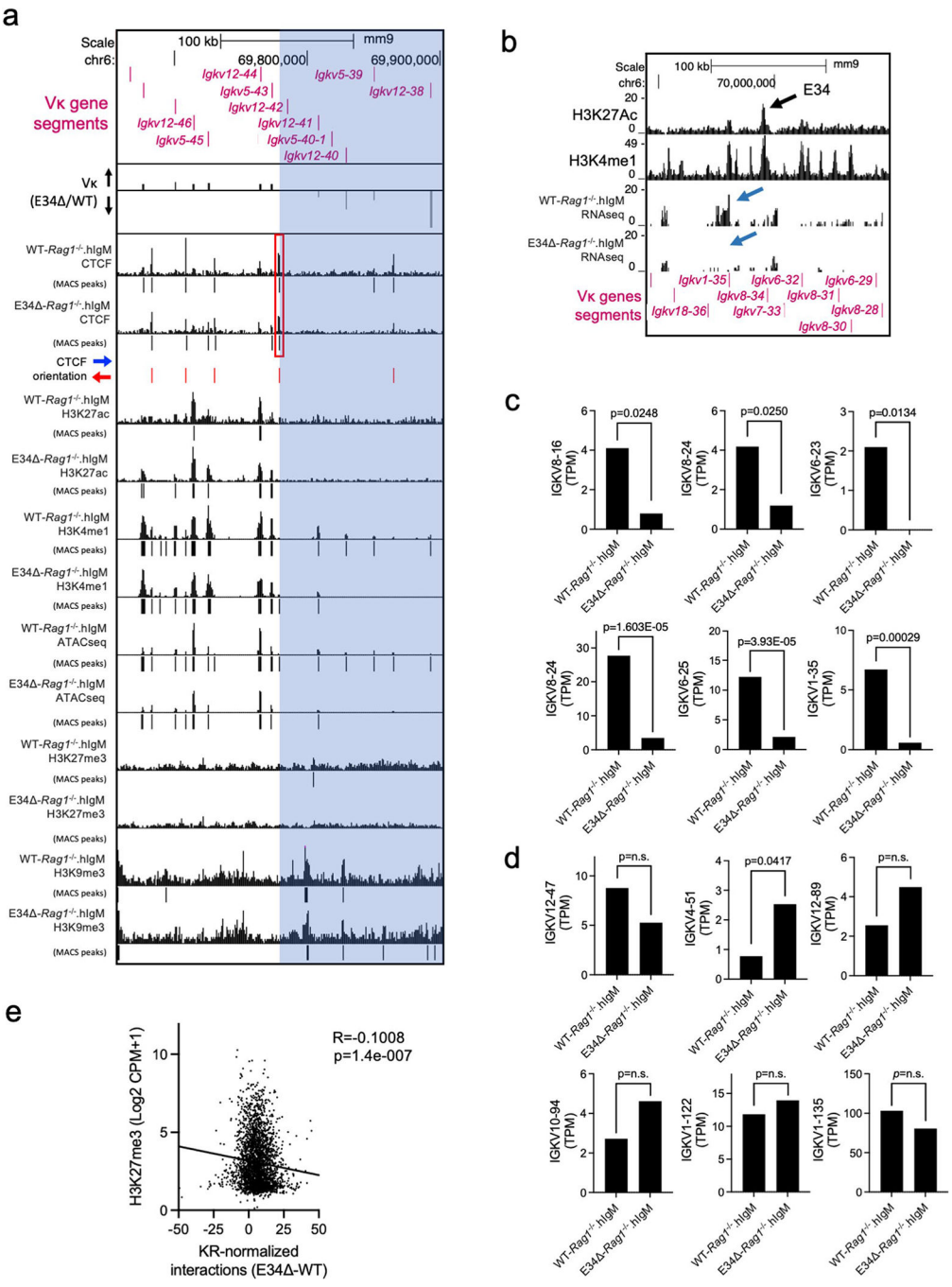

Extended Data Fig. 6 |. Igk locus non-coding transcription and epigenetic profiling at the 5′ boundary of the E34 subTAD in WT-*Rag1*$^{-/-}$.hIgM and E34Δ-*Rag1*$^{-/-}$.hIgM pre-B cells.
a, UCSC genome browser tracks spanning the Igk locus showing the deposition of CTCF, H3K27ac, H3K4me1, H3K27me3, and H3K9me3, as well as ATAC-seq reads in WT-*Rag1*$^{-/-}$.hIgM and E34Δ-*Rag1*$^{-/-}$.hIgM pre-B cells. Vκ rearrangement is also shown (E34Δ/WT). Significant peaks were called using MACS2 (Cutoff FDR < 0.05). The p-values cutoff for H3K9me3 reads was 0.001. Blue highlight indicates a genomic region downstream of the CTCF binding site affected by the E34 deletion. **b**, Genome browser view of the Igk locus centered on the E34 enhancer shows RNA-seq reads in WT-*Rag1*$^{-/-}$.hIgM and E34Δ-*Rag1*$^{-/-}$. hIgM pre-B cells. Blue arrows indicate affected transcripts. Tracks showing the deposition of H3K27Ac (GSM3103098) and H3K4me1 (GSM2084579) are shown. **c**, Non-coding transcripts expressed within the E34 subTAD with statistically significant changes are indicated. Data is expressed as Transcripts Per Million (TPM). DEseq analysis was used to calculate statistically significant changes for biological replicates. p-values are indicated. DEseq uses a negative binomial generalized linear model to determine significance of differences between transcript abundance. Data is derived from two independent experiment (two mice per group per genotype). **d**, Non-coding transcripts expressed in genomic regions located across the Igk locus but away from the E34 subTAD are shown. Data is derived from two independent experiment (two mice per group per genotype). DEseq analysis was used to calculate statistically significant changes in terms of p-values for biological replicates. p-values are indicated. DEseq uses a negative binomial generalized linear model to determine significance of differences between transcript abundance. **e**, Correlation between enrichment of H3K27me3 and KR-normalized interaction frequencies (E34Δ-WT) involving the E34 subTAD when compared to other genomic regions spanning chromosome 6 are indicated. Correlation coefficient (r) and p-values were calculated using simple linear regression.

Supplementary Material

Refer to Web version on PubMed Central for supplementary material.

Acknowledgements

Sequencing was performed at the IGM Genomics Center, University of California at San Diego, La Jolla, CA (grant no. P30CA023100). We thank Z. He for initiating HiC analysis. CRISPR mice were generated in the Transgenic Mouse Core at UCSD. This work, E.M.B-M. and H.L were supported by the NIH grant no. RO1 AI00880 (C.M.), grant no. AI09599 (C.M.), grant no. AI102853 (C.M.) and grant no. NSF-BSF 2019280 (C.M.). L.L. and M.H. were partially supported by grant no. R35HG011922. V.N., E.B. and J.A.V. were supported by grant no. U19 AI1427242–01. ARIMA Genomics contributed with reagents (Arima-HiC^{+} kit) in form of a grant awarded to E.M.B.-M.

Data availability

All data are available in the main text and extended data. Source data are provided with this paper. Sequencing data are accessible at GSE193968. No statistical methods were used to pre-determine sample sizes. Data distribution was assumed to be normal but this was not formally tested. No animals or data points were excluded from the analyses for any reason.

References

1. Schatz DG & Ji Y Recombination centres and the orchestration of V(D)J recombination. Nat. Rev. Immunol. 11, 251–263 (2011). [PubMed: 21394103]
2. Novobrantseva TI et al. Rearrangement and expression of immunoglobulin light chain genes can precede heavy chain expression during normal B cell development in mice. J. Exp. Med. 189, 75–88 (1999). [PubMed: 9874565]
3. Wong JB et al. B-1a cells acquire their unique characteristics by bypassing the pre-BCR selection stage. Nat. Commun. 10, 4768 (2019). [PubMed: 31628339]
4. Nemazee D Mechanisms of central tolerance for B cells. Nat. Rev. Immunol. 17, 281–294 (2017). [PubMed: 28368006]
5. Dixon JR et al. Topological domains in mammalian genomes identified by analysis of chromatin interactions. Nature 485, 376–380 (2012). [PubMed: 22495300]
6. Nora EP et al. Spatial partitioning of the regulatory landscape of the X-inactivation centre. Nature 485, 381–385 (2012). [PubMed: 22495304]
7. Jin F et al. A high-resolution map of the three-dimensional chromatin interactome in human cells. Nature 503, 290–294 (2013). [PubMed: 24141950]
8. Beagan JA & Phillips-Cremins JE On the existence and functionality of topologically associating domains. Nat. Genet. 52, 8–16 (2020). [PubMed: 31925403]
9. Phillips-Cremins JE et al. Architectural protein subclasses shape 3D organization of genomes during lineage commitment. Cell 153, 1281–1295 (2013). [PubMed: 23706625]
10. Schwarzer W et al. Two independent modes of chromatin organization revealed by cohesin removal. Nature 551, 51–56 (2017). [PubMed: 29094699]
11. Fudenberg G et al. Formation of chromosomal domains by loop extrusion. Cell Rep. 15, 2038–2049 (2016). [PubMed: 27210764]
12. Rao SSP et al. Cohesin loss eliminates all loop domains. Cell 171, 305–320.e24 (2017). [PubMed: 28985562]
13. Sanborn AL et al. Chromatin extrusion explains key features of loop and domain formation in wild-type and engineered genomes. Proc. Natl Acad. Sci. USA 112, E6456–E6465 (2015). [PubMed: 26499245]
14. Rao SS et al. A 3D map of the human genome at kilobase resolution reveals principles of chromatin looping. Cell 159, 1665–1680 (2014). [PubMed: 25497547]
15. Vos ESM et al. Interplay between CTCF boundaries and a super enhancer controls cohesin extrusion trajectories and gene expression. Mol. Cell 81, 3082–3095.e6 (2021). [PubMed: 34197738]
16. Liu NQ et al. WAPL maintains a cohesin loading cycle to preserve cell-type-specific distal gene regulation. Nat. Genet. 53, 100–109 (2021). [PubMed: 33318687]
17. Zhu Y, Denholtz M, Lu H & Murre C Calcium signaling instructs NIPBL recruitment at active enhancers and promoters via distinct mechanisms to reconstruct genome compartmentalization. Genes Dev. 35, 65–81 (2021). [PubMed: 33334824]
18. Denholtz M et al. Upon microbial challenge, human neutrophils undergo rapid changes in nuclear architecture and chromatin folding to orchestrate an immediate inflammatory gene program. Genes Dev. 34, 149–165 (2020). [PubMed: 31919189]
19. Ebert A, Hill L & Busslinger M Spatial regulation of V-(D)J recombination at antigen receptor loci. Adv. Immunol. 128, 93–121 (2015). [PubMed: 26477366]
20. Jhunjhunwala S, van Zelm MC, Peak MM & Murre C Chromatin architecture and the generation of antigen receptor diversity. Cell 138, 435–448 (2009). [PubMed: 19665968]
21. Qiu X et al. Sequential enhancer sequestration dysregulates recombination center formation at the IgH locus. Mol. Cell 70, 21–33.e6 (2018). [PubMed: 29576529]
22. Zhang Y, Zhang X, Dai HQ, Hu H & Alt FW The role of chromatin loop extrusion in antibody diversification. Nat. Rev. Immunol. 22, 550–566 (2022). [PubMed: 35169260]
23. Dai HQ et al. Loop extrusion mediates physiological Igh locus contraction for RAG scanning. Nature 590, 338–343 (2021). [PubMed: 33442057]

24. Ba Z et al. CTCF orchestrates long-range cohesin-driven V(D)J recombinational scanning. Nature 586, 305–310 (2020). [PubMed: 32717742]
25. Hill L et al. Wapl repression by Pax5 promotes V gene recombination by Igh loop extrusion. Nature 584, 142–147 (2020). [PubMed: 32612238]
26. Zhang Y et al. The fundamental role of chromatin loop extrusion in physiological V(D)J recombination. Nature 573, 600–604 (2019). [PubMed: 31511698]
27. Lin SG, Ba Z, Alt FW & Zhang Y RAG chromatin scanning during V(D)J recombination and chromatin loop extrusion are related processes. Adv. Immunol. 139, 93–135 (2018). [PubMed: 30249335]
28. Jain S, Ba Z, Zhang Y, Dai HQ & Alt FW CTCF-binding elements mediate accessibility of RAG substrates during chromatin scanning. Cell 174, 102–116.e14 (2018). [PubMed: 29804837]
29. Inlay M, Alt FW, Baltimore D & Xu Y Essential roles of the κ light chain intronic enhancer and 3′ enhancer in κ rearrangement and demethylation. Nat. Immunol. 3, 463–468 (2002). [PubMed: 11967540]
30. Gorman JR et al. The Igκ enhancer influences the ratio of Igκ versus Igλ B lymphocytes. Immunity 5, 241–252 (1996). [PubMed: 8808679]
31. Xu Y, Davidson L, Alt FW & Baltimore D Deletion of the Igκ light chain intronic enhancer/matrix attachment region impairs but does not abolish VκJκ rearrangement. Immunity 4, 377–385 (1996). [PubMed: 8612132]
32. Barajas-Mora EM et al. A B-cell-specific enhancer orchestrates nuclear architecture to generate a diverse antigen receptor repertoire. Mol. Cell 73, 48–60.e5 (2019). [PubMed: 30449725]
33. Barajas-Mora EM & Feeney AJ Enhancers as regulators of antigen receptor loci three-dimensional chromatin structure. Transcription 11, 37–51 (2020). [PubMed: 31829768]
34. Lin YC et al. Global changes in the nuclear positioning of genes and intra- and interdomain genomic interactions that orchestrate B cell fate. Nat. Immunol. 13, 1196–1204 (2012). [PubMed: 23064439]
35. Ribeiro de Almeida C et al. The DNA-binding protein CTCF limits proximal Vκ recombination and restricts κ enhancer interactions to the immunoglobulin κ light chain locus. Immunity 35, 501–513 (2011). [PubMed: 22035845]
36. Xiang Y, Park SK & Garrard WT Vκ gene repertoire and locus contraction are specified by critical DNase I hypersensitive sites within the Vκ-Jκ intervening region. J. Immunol. 190, 1819–1826 (2013). [PubMed: 23296705]
37. Xiang Y, Zhou X, Hewitt SL, Skok JA & Garrard WT A multifunctional element in the mouse *Igκ* locus that specifies repertoire and *Ig* loci subnuclear location. J. Immunol. 186, 5356–5366 (2011). [PubMed: 21441452]
38. Ribeiro de Almeida C, Hendriks RW & Stadhouders R Dynamic control of long-range genomic interactions at the immunoglobulin κ light-chain locus. Adv. Immunol. 128, 183–271 (2015). [PubMed: 26477368]
39. Stadhouders R et al. Pre-B cell receptor signaling induces immunoglobulin κ locus accessibility by functional redistribution of enhancer-mediated chromatin interactions. PLoS Biol. 12, e1001791 (2014). [PubMed: 24558349]
40. Matheson LS et al. Local chromatin features including PU.1 and IKAROS binding and H3K4 methylation shape the repertoire of immunoglobulin kappa genes chosen for V(D)J recombination. Front. Immunol. 8, 1550 (2017). [PubMed: 29204143]
41. Kleiman E, Loguercio S & Feeney AJ Epigenetic enhancer marks and transcription factor binding influence Vκ gene rearrangement in pre-B cells and pro-B cells. Front. Immunol. 9, 2074 (2018). [PubMed: 30271408]
42. Kadioglu A, Weiser JN, Paton JC & Andrew PW The role of *Streptococcus pneumoniae* virulence factors in host respiratory colonization and disease. Nat. Rev. Microbiol. 6, 288–301 (2008). [PubMed: 18340341]
43. Briles DE, Forman C, Hudak S & Claflin JL Anti-phosphorylcholine antibodies of the T15 idiotype are optimally protective against *Streptococcus pneumoniae*. J. Exp. Med. 156, 1177–1185 (1982). [PubMed: 7153709]

44. Mi QS et al. Highly reduced protection against *Streptococcus pneumoniae* after deletion of a single heavy chain gene in mouse. Proc. Natl Acad. Sci. USA 97, 6031–6036 (2000). [PubMed: 10811914]
45. Briles DE et al. Antiphosphocholine antibodies found in normal mouse serum are protective against intravenous infection with type 3 *Streptococcus pneumoniae*. J. Exp. Med. 153, 694–705 (1981). [PubMed: 7252411]
46. Heinz S, Romanoski CE, Benner C & Glass CK The selection and function of cell type-specific enhancers. Nat. Rev. Mol. Cell Biol. 16, 144–154 (2015). [PubMed: 25650801]
47. Mercer EM et al. Multilineage priming of enhancer repertoires precedes commitment to the B and myeloid cell lineages in hematopoietic progenitors. Immunity 35, 413–425 (2011). [PubMed: 21903424]
48. Heinz S et al. Simple combinations of lineage-determining transcription factors prime *cis*-regulatory elements required for macrophage and B cell identities. Mol. Cell 38, 576–589 (2010). [PubMed: 20513432]
49. Brekke KM & Garrard WT Assembly and analysis of the mouse immunoglobulin kappa gene sequence. Immunogenetics 56, 490–505 (2004). [PubMed: 15378297]
50. Nussenzweig MC et al. Allelic exclusion in transgenic mice that express the membrane form of immunoglobulin μ. Science 236, 816–819 (1987). [PubMed: 3107126]
51. Denker A & de Laat W The second decade of 3C technologies: detailed insights into nuclear organization. Genes Dev. 30, 1357–1382 (2016). [PubMed: 27340173]
52. Karki S et al. Regulated capture of Vκ gene topologically associating domains by transcription factories. Cell Rep. 24, 2443–2456 (2018). [PubMed: 30157436]
53. Crane E et al. Condensin-driven remodelling of X chromosome topology during dosage compensation. Nature 523, 240–244 (2015). [PubMed: 26030525]
54. Kaul A, Bhattacharyya S & Ay F Identifying statistically significant chromatin contacts from Hi-C data with FitHiC2. Nat. Protoc. 15, 991–1012 (2020). [PubMed: 31980751]
55. Kubo N et al. Promoter-proximal CTCF binding promotes distal enhancer-dependent gene activation. Nat. Struct. Mol. Biol. 28, 152–161 (2021). [PubMed: 33398174]
56. Schmitt AD et al. A compendium of chromatin contact maps reveals spatially active regions in the human genome. Cell Rep. 17, 2042–2059 (2016). [PubMed: 27851967]
57. Knight PA & Ruiz D A fast algorithm for matrix balancing. IMA J. Numer. Anal. 33, 1029–1047 (2012).
58. Lieberman-Aiden E et al. Comprehensive mapping of long-range interactions reveals folding principles of the human genome. Science 326, 289–293 (2009). [PubMed: 19815776]
59. Cobb RM, Oestreich KJ, Osipovich OA & Oltz EM Accessibility control of V(D)J recombination. Adv. Immunol. 91, 45–109 (2006). [PubMed: 16938538]
60. Bolland DJ et al. Two mutually exclusive local chromatin states drive efficient V(D)J recombination. Cell Rep. 15, 2475–2487 (2016). [PubMed: 27264181]
61. Pulivarthy SR et al. Regulated large-scale nucleosome density patterns and precise nucleosome positioning correlate with V(D)J recombination. Proc. Natl Acad. Sci. USA 113, E6427–E6436 (2016). [PubMed: 27698124]
62. Carico Z & Krangel MS Chromatin dynamics and the development of the TCRα and TCRδ repertoires. Adv. Immunol. 128, 307–361 (2015). [PubMed: 26477370]
63. Lam JH & Baumgarth N The multifaceted B cell response to influenza virus. J. Immunol. 202, 351–359 (2019). [PubMed: 30617116]
64. Bossen C et al. The chromatin remodeler Brg1 activates enhancer repertoires to establish B cell identity and modulate cell growth. Nat. Immunol. 16, 775–784 (2015). [PubMed: 25985234]
65. Johanson TM et al. Transcription-factor-mediated supervision of global genome architecture maintains B cell identity. Nat. Immunol. 19, 1257–1264 (2018). [PubMed: 30323344]
66. Sakamoto S et al. E2A and CBP/p300 act in synergy to promote chromatin accessibility of the immunoglobulin κ locus. J. Immunol. 188, 5547–5560 (2012). [PubMed: 22544934]

67. Goebel P et al. Localized gene-specific induction of accessibility to V(D)J recombination induced by E2A and early B cell factor in nonlymphoid cells. J. Exp. Med. 194, 645–656 (2001). [PubMed: 11535632]
68. Cobaleda C, Schebesta A, Delogu A & Busslinger M Pax5: the guardian of B cell identity and function. Nat. Immunol. 8, 463–470 (2007). [PubMed: 17440452]
69. Abarrategui I & Krangel MS Regulation of T cell receptor-α gene recombination by transcription. Nat. Immunol. 7, 1109–1115 (2006). [PubMed: 16936730]
70. Schlissel MS & Baltimore D Activation of immunoglobulin kappa gene rearrangement correlates with induction of germline kappa gene transcription. Cell 58, 1001–1007 (1989). [PubMed: 2505932]
71. Khanna N, Zhang Y, Lucas JS, Dudko OK & Murre C Chromosome dynamics near the sol-gel phase transition dictate the timing of remote genomic interactions. Nat. Com. 10, 2771 (2019).
72. Hansen AS et al. Distinct classes of chromatin loops revealed by deletion of an RNA-binding region in CTCF. Mol. Cell 76, 395–411 e313 (2019). [PubMed: 31522987]
73. Wang H et al. Widespread plasticity in CTCF occupancy linked to DNA methylation. Genome Res. 22, 1680–1688 (2012). [PubMed: 22955980]
74. Saldana-Meyer R et al. RNA interactions are essential for CTCF-mediated genome organization. Mol. Cell 76, 412–422 e415 (2019). [PubMed: 31522988]
75. Young NM, Foote SJ & Wakarchuk WW Review of phosphocholine substituents on bacterial pathogen glycans: synthesis, structures and interactions with host proteins. Mol. Immunol. 56, 563–573 (2013). [PubMed: 23911414]
76. Holodick NE, Rodriguez-Zhurbenko N & Hernandez AM Defining natural antibodies. Front. Immunol. 8, 872 (2017). [PubMed: 28798747]
77. Vas J, Gronwall C & Silverman GJ Fundamental roles of the innate-like repertoire of natural antibodies in immune homeostasis. Front. Immunol. 4, 4 (2013). [PubMed: 23386848]
78. Hoebinger C, Rajcic D & Hendrikx T Oxidized lipids: common immunogenic drivers of non-alcoholic fatty liver disease and atherosclerosis. Front. Cardiovasc. Med. 8, 824481 (2021). [PubMed: 35083304]
79. Sun X et al. Neutralization of oxidized phospholipids ameliorates non-alcoholic steatohepatitis. Cell Metab. 31, 189–206 e188 (2020). [PubMed: 31761566]
80. Que X et al. Oxidized phospholipids are proinflammatory and proatherogenic in hypercholesterolaemic mice. Nature 558, 301–306 (2018). [PubMed: 29875409]
81. Zou J, Wang G, Li H, Yu X & Tang C IgM natural antibody T15/E06 in atherosclerosis. Clin. Chim. Acta 504, 15–22 (2020). [PubMed: 31991130]
82. Shaw PX et al. Natural antibodies with the T15 idiotype may act in atherosclerosis, apoptotic clearance, and protective immunity. J. Clin. Invest. 105, 1731–1740 (2000). [PubMed: 10862788]
83. Dosenovic P et al. Anti-HIV-1 B cell responses are dependent on B cell precursor frequency and antigen-binding affinity. Proc. Natl Acad. Sci. USA 115, 4743–4748 (2018). [PubMed: 29666227]
84. Abbott RK et al. Precursor frequency and affinity determine B cell competitive fitness in germinal centers, tested with germline-targeting HIV vaccine immunogens. Immunity 48, 133–146.e6 (2018). [PubMed: 29287996]
85. Taylor JJ, Pape KA, Steach HR & Jenkins MK Humoral immunity. Apoptosis and antigen affinity limit effector cell differentiation of a single naïve B cell. Science 347, 784–787 (2015). [PubMed: 25636798]
86. Sangesland M et al. Germline-encoded affinity for cognate antigen enables vaccine amplification of a human broadly neutralizing response against influenza virus. Immunity 51, 735–749.e8 (2019). [PubMed: 31563464]
87. Claringbould A & Zaugg JB Enhancers in disease: molecular basis and emerging treatment strategies. Trends Mol. Med. 27, 1060–1073 (2021). [PubMed: 34420874]
88. Kenter AL, Watson CT & Spille JH Igh locus polymorphism may dictate topological chromatin conformation and V gene usage in the Ig repertoire. Front. Immunol. 12, 682589 (2021). [PubMed: 34084176]

89. Watson CT & Breden F The immunoglobulin heavy chain locus: genetic variation, missing data, and implications for human disease. Genes Immun. 13, 363–373 (2012). [PubMed: 22551722]

90. Mikocziova I, Greiff V & Sollid LM Immunoglobulin germline gene variation and its impact on human disease. Genes Immun. 22, 205–217 (2021). [PubMed: 34175903]

91. Bolotin DA et al. MiXCR: software for comprehensive adaptive immunity profiling. Nat. Methods 12, 380–381 (2015). [PubMed: 25924071]

92. Dixon JR et al. Chromatin architecture reorganization during stem cell differentiation. Nature 518, 331–336 (2015). [PubMed: 25693564]

93. Zhang Y et al. Transcriptionally active HERV-H retrotransposons demarcate topologically associating domains in human pluripotent stem cells. Nat. Genet. 51, 1380–1388 (2019). [PubMed: 31427791]

94. Durand NC et al. Juicer provides a one-click system for analyzing loop-resolution Hi-C experiments. Cell Syst. 3, 95–98 (2016). [PubMed: 27467249]

95. Yang T et al. HiCRep: assessing the reproducibility of Hi-C data using a stratum-adjusted correlation coefficient. Genome Res. 27, 1939–1949 (2017). [PubMed: 28855260]

96. Hainer SJ & Fazzio TG High-resolution chromatin profiling using CUT&RUN. Curr. Protoc. Mol. Biol. 126, e85 (2019). [PubMed: 30688406]

97. Lemoine F et al. NGPhylogeny.fr: new generation phylogenetic services for non-specialists. Nucleic Acids Res. 47, W260–W265 (2019). [PubMed: 31028399]

98. Lemoine F et al. Renewing Felsenstein's phylogenetic bootstrap in the era of big data. Nature 556, 452–456 (2018). [PubMed: 29670290]

99. Letunic I & Bork P Interactive Tree Of Life (iTOL) v5: an online tool for phylogenetic tree display and annotation. Nucleic Acids Res. 49, W293–W296 (2021). [PubMed: 33885785]

100. Katoh K & Standley DM MAFFT multiple sequence alignment software version 7: improvements in performance and usability. Mol. Biol. Evol. 30, 772–780 (2013). [PubMed: 23329690]

101. Lefort V, Desper R & Gascuel O FastME 2.0: a comprehensive, accurate, and fast distance-based phylogeny inference program. Mol. Biol. Evol. 32, 2798–2800 (2015). [PubMed: 26130081]

102. Criscuolo A & Gribaldo S BMGE (Block Mapping and Gathering with Entropy): a new software for selection of phylogenetic informative regions from multiple sequence alignments. BMC Evol. Biol. 10, 210 (2010). [PubMed: 20626897]

103. Desper R & Gascuel O Fast and accurate phylogeny reconstruction algorithms based on the minimum-evolution principle. J. Comput. Biol. 9, 687–705 (2002). [PubMed: 12487758]

104. Afgan E et al. The Galaxy platform for accessible, reproducible and collaborative biomedical analyses: 2018 update. Nucleic Acids Res. 46, W537–W544 (2018). [PubMed: 29790989]

105. Langmead B & Salzberg SL Fast gapped-read alignment with Bowtie 2. Nat. Methods 9, 357–359 (2012). [PubMed: 22388286]

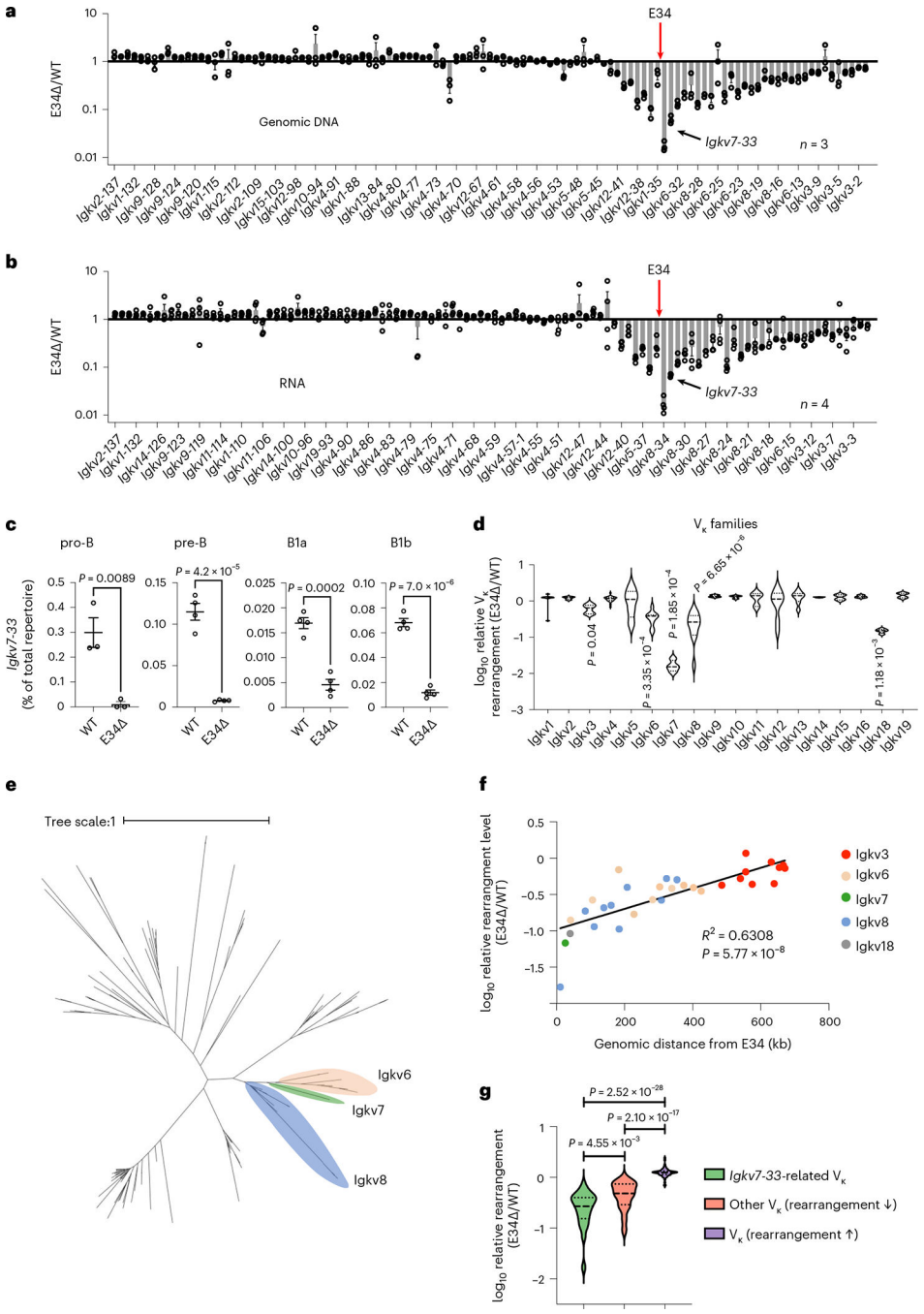

Fig. 1 |. An enhancer that instructs *Igkv7–33* gene rearrangement.

a, Relative Vκ gene rearrangement frequencies, using genomic DNA (gDNA) as starting material, in WT and E34Δ adult bone marrow pre-B cells are shown. **b**, Relative V_{κ} gene rearrangement frequencies, using RNA as starting material, in WT and E34Δ adult bone marrow pre-B cells are shown. RNA and gDNA were derived from WT and E34Δ adult bone marrow pre-B cells and analyzed for V_{κ} gene usage. Data were derived from three (gDNA) and four (RNA) independent experiments using one mouse for each genotype per experiment and are expressed as the ratio of gene usage in E34Δ versus WT pre-B

cells ± s.e.m. **c**, Levels of *Igkv7–33* rearrangements in pro-B, pre-B, B1a and B1b B cells derived from E34Δ or littermate (WT) mice. Data were derived from three (pro-B) and four (pre-B, B1a and B1b) independent experiments and are expressed as a percentage of the total number of reads ± s.e.m. Significant differences between groups were assessed using an unpaired *t*-test. **d**, Violin plots show relative rearrangement frequencies in E34Δ and littermate (WT) pre-B cells for indicated V_κ gene families. Dashes and dotted lines represent means and quartiles, respectively. Significant differences between each group with reduced rearrangement and the combined data from all groups were assessed using an unpaired *t*-test. **e**, Phylogenetic analysis of functional V_κ genes. Indicated are families most affected by the E34 deletion with the exception of the Igkv18 family. The distance scale represents the percentage of genetic variation between the sequences. **f**, Correlation between the genomic distance and relative levels of rearrangement among the V_κ gene families that showed significantly reduced rearrangement frequencies. Correlation coefficient (*r*) and *P* values were calculated using simple linear regression. **g**, Violin plots showing the relative frequencies of rearrangements between genetically *Igkv7–33*-related V_κ genes (green), non-*Igkv7–33*-related V_κ genes associated with reduced rearrangement frequencies (orange) and V_κ genes linked with increased rearrangement frequencies (purple). Significant differences between groups were assessed using an unpaired *t*-test. Dashes and dotted lines represent means and quartiles, respectively. Rearrangement frequencies for **a**, **b** and **f** are shown as averages of the ratio of E34Δ versus littermate controls (WT).

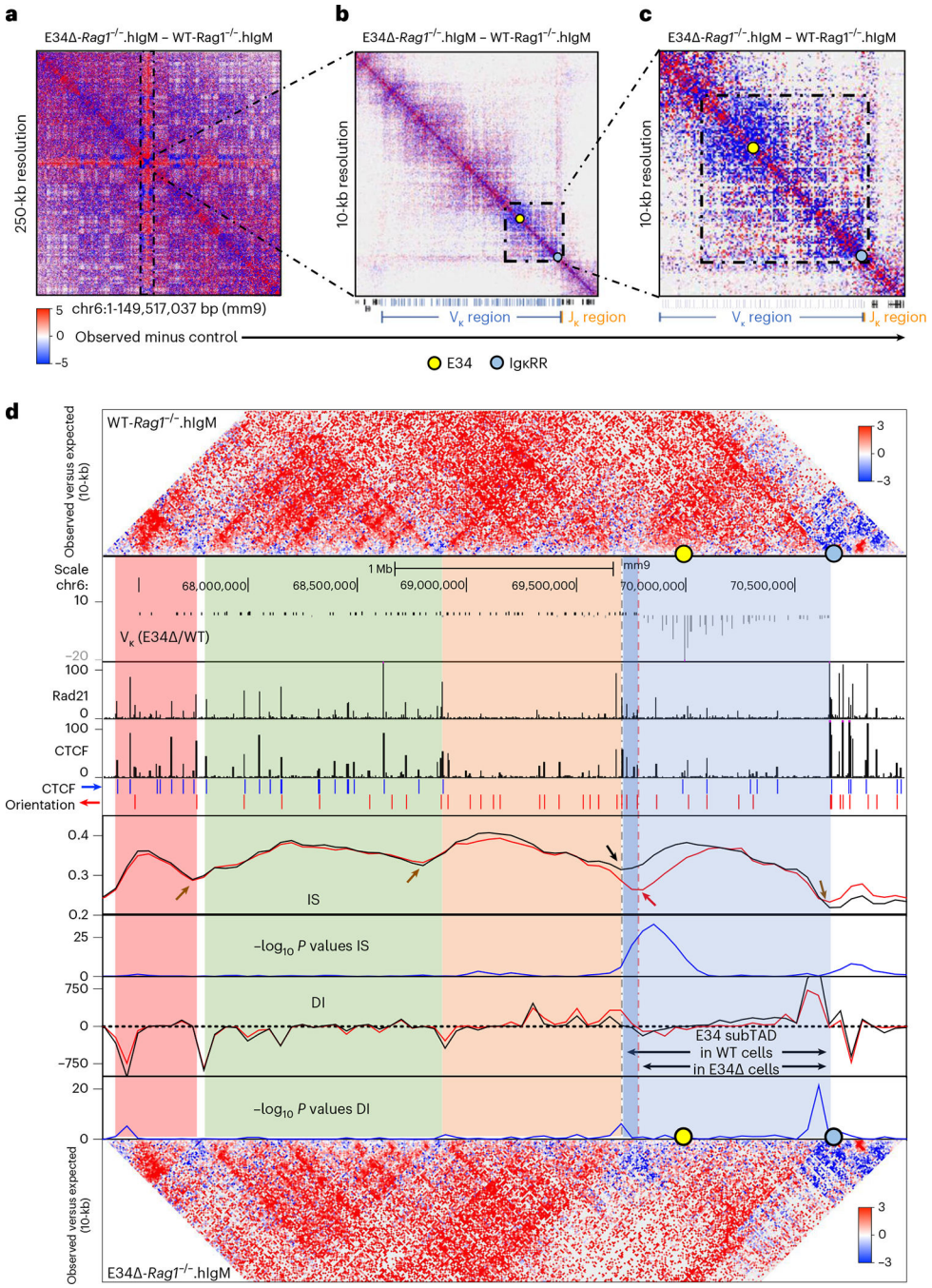

Fig. 2 |. The E34 enhancer instructs changes in chromatin folding and boundary elements.
a–**c**, HiC matrix differential contact heatmaps showing chromatin interaction frequencies in WT-*Rag1*$^{-/-}$.hIgM and E34Δ-*Rag1*$^{-/-}$. hIgM pre-B cells for: chromosome 6 (**a**), the Igk locus (**b**) and a genomic region spanning the E34 enhancer (**c**). Indicated are the locations of the E34 enhancer (yellow dot) and the Igκ**κ**RR (blue dot). Data are derived from two independent experiments using four mice each in experiment 1 and two mice each for experiment 2. **d**, HiC contact matrices for WT-*Rag1*$^{-/-}$.hIgM (top) and E34Δ-*Rag1*$^{-/-}$.hIgM (bottom) pre-B cells. Heatmaps indicate normalized interaction frequencies. Indicated are

the locations of the E34 enhancer (yellow dot) and the IgκRR (blue dot). Black lines indicate IS and DI scores associated with the genomes derived from WT-*Rag1*$^{-/-}$.hIgM pre-B cells. Red lines indicate IS and DI scores associated with the genomes derived from E34Δ-*Rag1*$^{-/-}$.hIgM pre-B cells. Shown are tracks indicating V_{κ} rearrangement (E34Δ/WT), Rad21 occupancy (GSM2973688), CTCF occupancy (GSM2973687) and CTCF binding orientation (blue and red arrows). Shown are IS and the DI. Brown arrows indicate unaltered DI scores or potential boundaries segregating subTADs for WT-*Rag1*$^{-/-}$.hIgM versus E34Δ-*Rag1*$^{-/-}$.hIgM pre-B cells. Black and red arrows indicate a boundary element segregating two subTADs in WT-*Rag1*$^{-/-}$.hIgM and E34Δ-*Rag1*$^{-/-}$.hIgM pre-B cells, respectively. SubTADs were identified using DI and IS as well as CTCF-marked boundary elements. SubTADs are highlighted by color. The genomic region spanning the E34 subTAD in WT-*Rag1*$^{-/-}$.hIgM pre-B cells is highlighted in light and dark blue. Light-blue highlight indicates the E34 subTAD in E34Δ-*Rag1*$^{-/-}$.hIgM pre-B cells. Tracks show $-\log_{10} P$ values for IS and DI scores for WT-*Rag1*$^{-/-}$.hIgM versus E34Δ-*Rag1*$^{-/-}$.hIgM pre-B cells (blue lines). A two-sided *Z*-test was used to calculate *P* values.

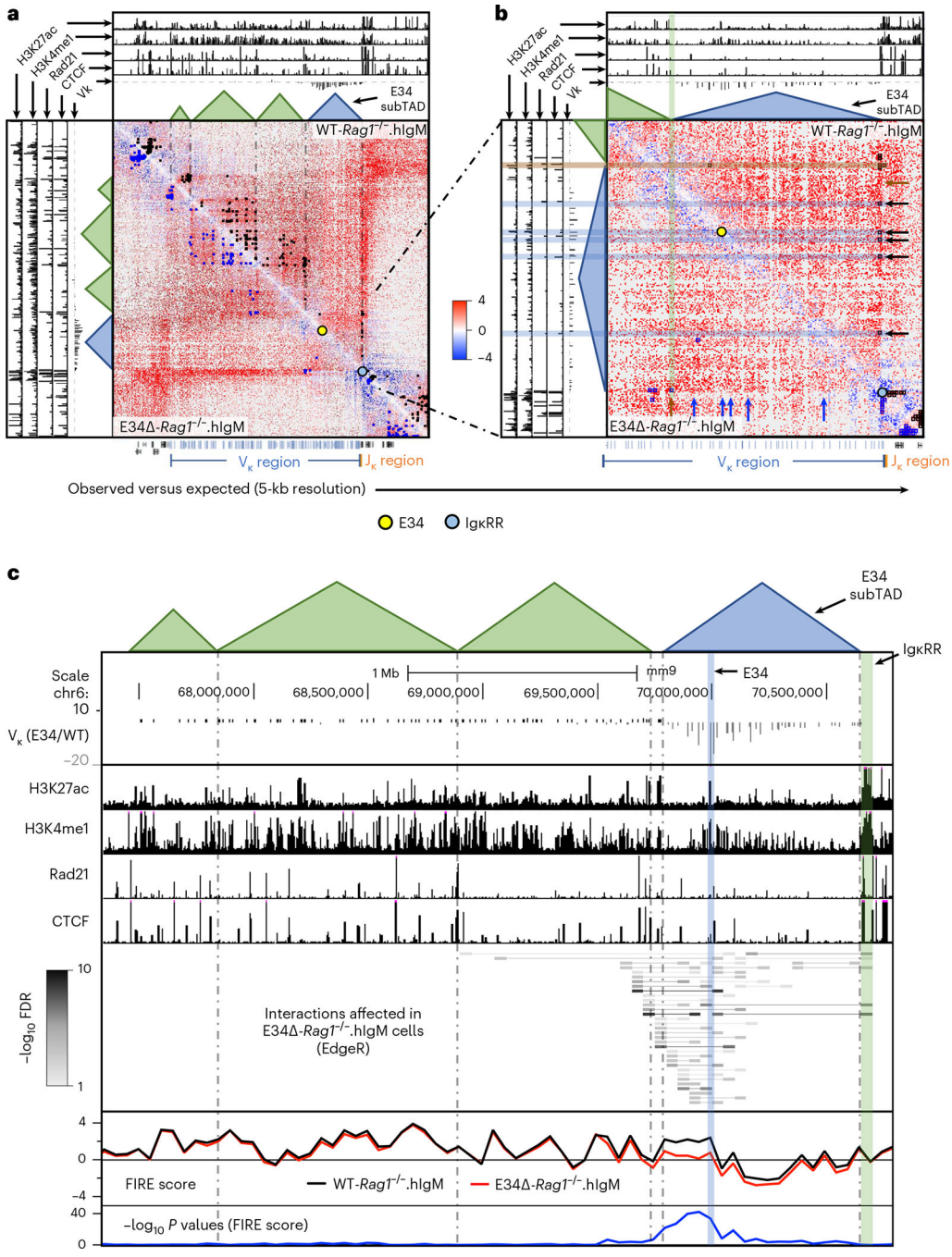

Fig. 3 |. The E34 enhancer instructs the chromatin interaction landscape across the Igk locus.
a, HiC matrix contact heatmaps for a genomic region around the Igk locus in WT-*Rag1*$^{-/-}$.hIgM and E34Δ-*Rag1*$^{-/-}$.hIgM pre-B cells are shown. **b**, HiC matrix contact heatmaps for a genomic region located in the vicinity of the E34 enhancer in WT-*Rag1*$^{-/-}$.hIgM and E34Δ-*Rag1*$^{-/-}$.hIgM pre-B cells are shown. Tracks show the deposition of H3K27ac, H3K4me1, Rad21 and CTCF as well as relative V_{κ} rearrangement frequencies (E34Δ/WT). Indicated are chromatin interactions detected by FitHiC2 in WT-*Rag1*$^{-/-}$.hIgM (black dots) and E34Δ-*Rag1*$^{-/-}$.hIgM (blue dots) cells. Bottom shows the location of the

V_κ (blue), J_κ (orange) and other gene segments (black). Yellow and blue dots indicate the genomic locations of the E34 enhancer and the IgκRR, respectively. **c**, Chromatin interactions affected by the E34 deletion across the Igk locus were analyzed using EdgeR (50-kb resolution). The E34 enhancer, the IgκRR and subTADs that span the Igk locus are indicated. Tracks show relative V_κ rearrangement frequencies (E34Δ/WT) and the deposition of H3K27ac, H3K4me1, Rad21 and CTCF. Gray scale represents negative $\log_{10}$ *P* values for each interaction as revealed using EdgeR. FIRE scores calculated for WT-*Rag1*$^{-/-}$.hIgM and E34Δ-*Rag1*$^{-/-}$.hIgM pre-B cells are indicated. Significant differences for FIRE scores between WT-*Rag1*$^{-/-}$.hIgM and E34Δ-*Rag1*$^{-/-}$.hIgM pre-B cells are shown as negative $\log_{10}$ *P* values and were calculated using a two-sided *Z*-test. FDR, false discovery rate.

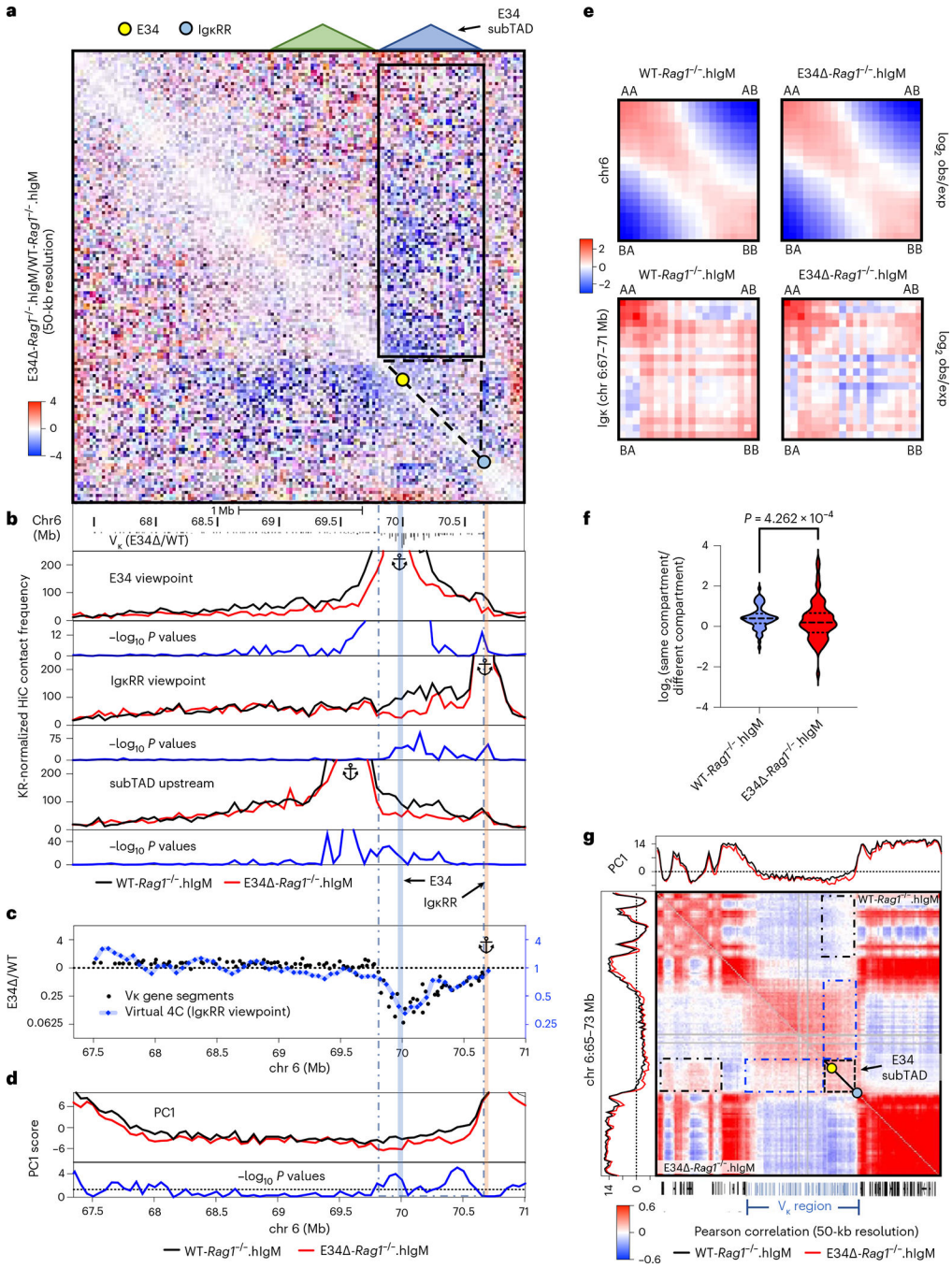

Fig. 4 |. The E34 enhancer instructs insulation and compartmentalization of the E34 subTAD.

a, HiC contact matrix heatmap for contact frequencies (E34Δ/WT) for WT-*Rag1*$^{-/-}$.hIgM versus E34Δ-*Rag1*$^{-/-}$.hIgM pre-B cells. Indicated are the Igk subTADs. **b**, Virtual 4C plots are shown for WT-*Rag1*$^{-/-}$.hIgM and E34Δ-*Rag1*$^{-/-}$.hIgM pre-B cells. Interactions emanating from the E34, Igκ RR and a subTAD located adjacent to the E34 subTAD are shown. Indicated are the locations of the E34 (blue highlight) and Igκ RR (beige highlight). Negative $\log_{10}$ *P* values indicating significant differences between WT-*Rag1*$^{-/-}$.hIgM versus E34Δ-*Rag1*$^{-/-}$.hIgM pre-B cells are shown (blue lines). **c**, Correlations between the relative

chromatin contact frequencies involving the IgκRR ($J_κ$ genes), $V_κ$ gene segment location and $V_κ$ rearrangement levels are indicated. Virtual 4C track emanating from the IgκRR viewpoint (50-kb resolution) using a moving average of three genomic regions from the ratio of WT-*Rag1*$^{-/-}$.hIgM versus E34Δ-*Rag1*$^{-/-}$.hIgM is shown (right *y* axis in blue). $V_κ$ gene rearrangement is expressed as the ratio of WT versus E34Δ pre-B cells. **d**, PC1 scores of HiC data derived from WT-*Rag1*$^{-/-}$.hIgM and E34Δ-*Rag1*$^{-/-}$.hIgM pre-B cells are shown. Negative $\log_{10}$ *P* values indicating significant differences between WT-*Rag1*$^{-/-}$.hIgM and E34Δ-*Rag1*$^{-/-}$.hIgM pre-B cells are shown (blue lines). **e**, Saddle plots indicating compartmentalization strength in WT-*Rag1*$^{-/-}$.hIgM and E34Δ-*Rag1*$^{-/-}$.hIgM pre-B cells spanning chromosome 6 (top matrices) and the Igk locus (bottom matrices) are shown. Averaged distance-normalized contact frequencies between *cis* pairs of genomic bins were arranged by changing PC1 values. **f**, Violin plots comparing distributions of $\log_2$ ratios for averaged genomic interaction frequencies involving different compartments are shown for WT-*Rag1*$^{-/-}$.hIgM and E34Δ-*Rag1*$^{-/-}$.hIgM pre-B cells. Statistical analyses of changes were calculated using a paired *t*-test. **g**, Pearson correlation matrices for HiC reads derived from WT-*Rag1*$^{-/-}$.hIgM and E34Δ-*Rag1*$^{-/-}$.hIgM pre-B cells are shown at 50-kb resolution. Blue and black dashed interrupted rectangles indicate changes in compartment association involving the E34 subTAD (black triangles) with genomic regions located across the Igk locus and genomic regions positioned outside the Igk locus, respectively. Yellow and blue dots indicate the E34 enhancer and the IgκRR, respectively. obs/exp, observed divided expected.

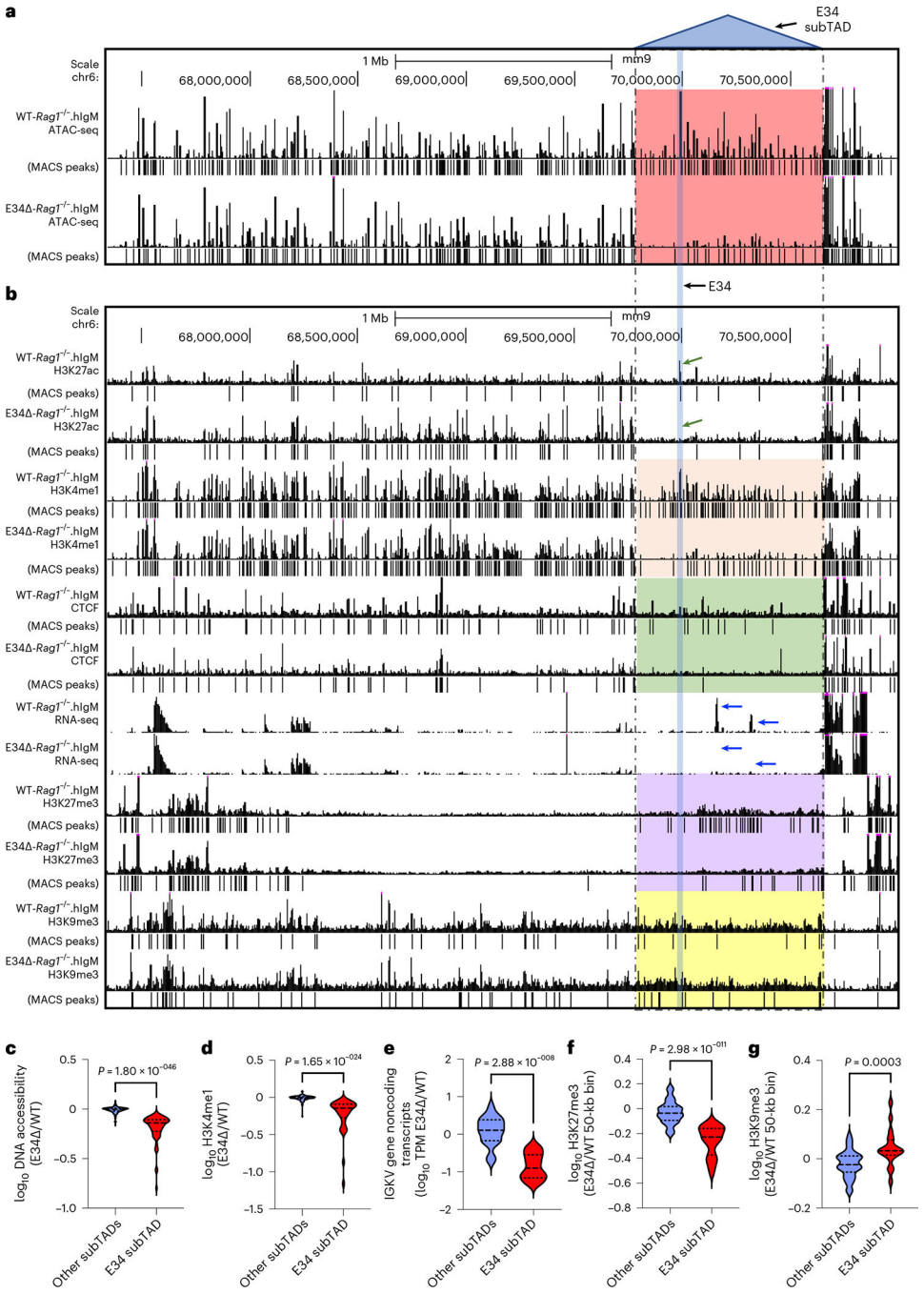

Fig. 5 |. The E34 enhancer instructs chromatin accessibility, the deposition of activating histone marks, CTCF occupancy and noncoding transcription across the E34 subTAD.

a, UCSC Genome Browser tracks spanning the Igk locus showing ATAC-seq reads for WT-*Rag1*$^{-/-}$.hIgM and E34Δ-*Rag1*$^{-/-}$.hIgM pre-B cells. **b**, UCSC Genome Browser tracks spanning the Igk locus show the deposition of H3K27ac, H3K4me1, H3K27me3 and H3K9me3 in WT-*Rag1*$^{-/-}$.hIgM and E34Δ-*Rag1*$^{-/-}$.hIgM pre-B cells. CTCF occupancy and RNA-seq reads are also shown for WT-*Rag1*$^{-/-}$.hIgM and E34Δ-*Rag1*$^{-/-}$.hIgM pre-B cells. Significant peaks were called using MACS2 (cutoff FDR < 0.05). The *P* value threshold for

H3K9me3 abundance was 0.001. Indicated (dashed lines) is the location of the E34 subTAD. Blue arrows indicate noncoding transcripts associated with the E34 subTAD expressed in WT-*Rag1*$^{-/-}$.hIgM and E34Δ-*Rag1*$^{-/-}$.hIgM pre-B cells, respectively. **c**, Fold changes in peak enrichment for chromatin accessibility (ATAC-seq reads) across the E34 subTAD and the rest of the lgk locus are indicated. **d**, Fold changes in peak enrichment for H3K4me1 abundance across the E34 subTAD and the rest of the lgk locus are indicated. **e**, Fold changes in V-gene noncoding transcript abundance, expressed as transcripts per million (TPM), within the E34 subTAD as well as other subTADs that span the rest of the lgk locus are indicated. **f**, Fold changes in H3K27me3 enrichment per 50-kb bin within the E34 subTAD and the rest of the lgk locus are shown. **g**, Fold changes in H3K9me3 enrichment per 50-kb bin within the E34 subTAD and the rest of the lgk locus are shown. Significant differences between groups in **c**–**g** were computed using an unpaired Student's *t*-test. Data shown were derived from two independent experiments using four mice per group.

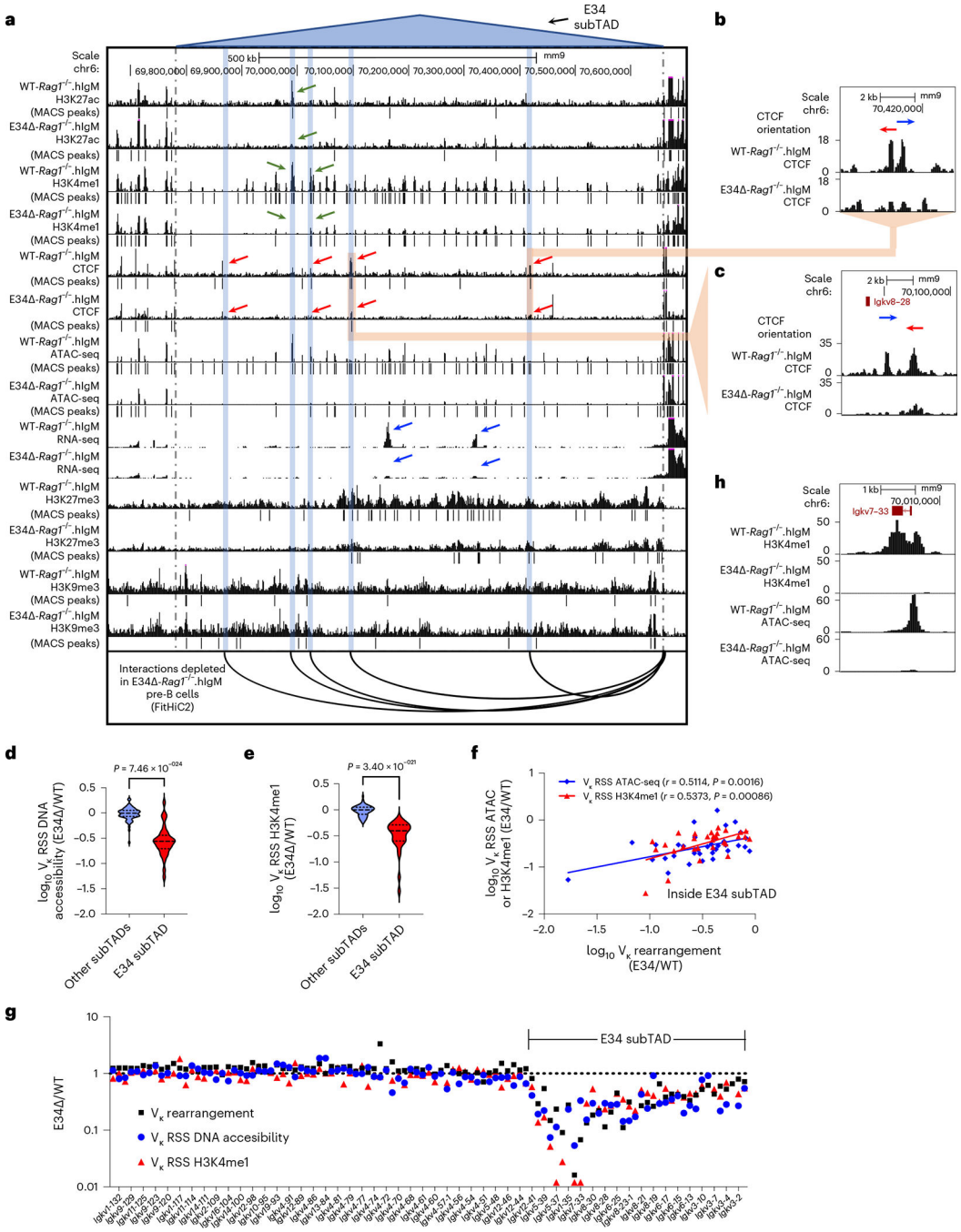

Fig. 6 |. The E34 enhancer instructs the deposition of epigenetic marks at genomic regions associated with Igk locus chromatin folding and V_κ-J_κ rearrangement.

a, UCSC Genome Browser tracks show the deposition of H3K27ac, H3K4me1, CTCF, H3K27me3 and H3K9me3 across the E34 subTAD in WT-*Rag1*$^{-/-}$.hIgM and E34Δ-*Rag1*$^{-/-}$.hIgM pre-B cells. ATAC-seq and RNA-seq reads for WT-*Rag1*$^{-/-}$.hIgM and E34Δ-*Rag1*$^{-/-}$.hIgM pre-B cells are also shown. Significant peaks were called using MACS2 (cutoff FDR < 0.05). The *P* value threshold for H3K9me3 abundance was 0.001. Blue highlights indicate the location of the chromatin interactions depleted in E34Δ-*Rag1*$^{-/-}$.hIgM pre-B cells as

compared with WT-*Rag1*$^{-/-}$.hIgM pre-B cells using the Igκ RR as a viewpoint. **b**, Shown are CTCF binding sites involved in chromatin interactions proximal to the CER element affected in E34Δ-*Rag1*$^{-/-}$.hIgM pre-B cells when compared with WT-*Rag1*$^{-/-}$.hIgM pre-B cells. **c**, Shown are CTCF binding sites involved in chromatin interactions near the *Igkv8–28* gene segment affected in E34Δ-*Rag1*$^{-/-}$. hIgM pre-B cells when compared with WT-*Rag1*$^{-/-}$.hIgM pre-B cells. **d**, Fold changes in chromatin accessibility at the RSSs of $V_κ$ genes located within the E34 subTAD and subTADs that span the rest of the lgk locus are shown. **e**, Fold changes in H3K4me1 enrichment at the RSSs of Vκ genes located within the E34 subTAD and subTADs that span the rest of the lgk locus are shown. Significant differences between groups in **d** and **e** were calculated using an unpaired Student's *t*-test. **f**, Correlation between $V_κ$ rearrangement frequencies, DNA accessibility and H3K4me1 enrichment at the $V_κ$ RSS is indicated. Correlation coefficients (*r*) and *P* values were calculated using simple linear regression. **g**, Fold changes in Vκ rearrangement frequencies, DNA accessibility and H3K4me1 enrichment at the Vκ RSS are shown. **h**, Chromatin accessibility and H3K4me1 abundance across the *Igkv7–33* gene are shown.

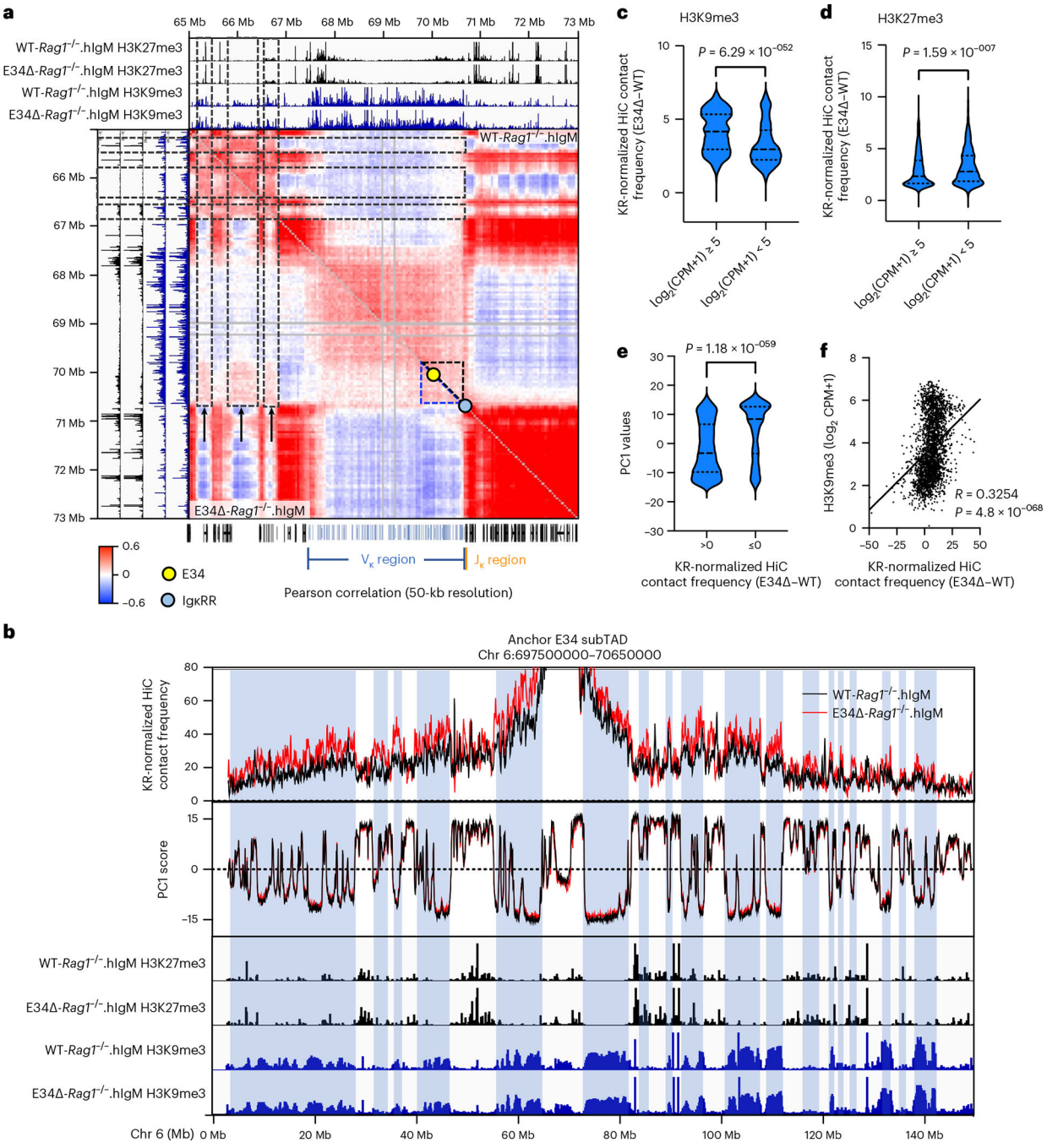

Fig. 7 |. The E34 enhancer impedes recruitment of the E34 subTAD to pericentromeric heterochromatin.

a, HiC Pearson correlation matrices derived from WT-*Rag1*$^{-/-}$.hIgM and E34Δ-*Rag1*$^{-/-}$.hIgM pre-B cells are shown at 50-kb resolution. Included are tracks for H3K27me3 and H3K9me3 abundance in WT-*Rag1*$^{-/-}$.hIgM and E34Δ-*Rag1*$^{-/-}$.hIgM pre-B cells. Dashed black rectangles show correlation between de novo chromatin interactions emanating from the E34 subTAD in E34Δ-*Rag1*$^{-/-}$.hIgM pre-B cells (black arrows) and genomic regions deposited by transcriptionally repressive epigenetic marks. The E34 subTAD is shown as

dashed triangles. Yellow and blue dots indicate the locations of the E34 enhancer and the Igκ RR. **b**, Virtual 4C plots using the E34 subTAD as a viewpoint across chromosome 6 are indicated. PC1 scores and deposition of H3K27me3 and H3K9me3 are shown. Blue highlights indicate correlation between chromatin interactions emanating from the E34 subTAD, negative PC1 values and genomic regions associated with the deposition of transcriptional repressive marks. Virtual 4C plots were plotted at 50-kb resolution using a moving average of three genomic (50-kb) regions. One representative set of H3K27me3 and H3K9me3 reads derived from two independent experiments was plotted. **c**, Statistical analyses correlating enrichment of H3K9me3 abundance in counts per million (CPM) and KR-normalized HiC contact frequencies are shown. **d**, Statistical analyses correlating enrichment of H3K27me3 abundance in counts per million (CPM) and KR-normalized HiC contact frequencies are shown. **e**, Statistical analyses of correlation between PC1 values and the KR-normalized HiC contact frequencies (E34Δ–WT) are indicated. Significant differences between groups in **c**–**e** were calculated using an unpaired *t*-test. **f**, Correlations between H3K9me3 abundance and KR-normalized HiC contact frequencies (E34Δ–WT) are shown. Correlation coefficient (*r*) and *P* values were calculated using simple linear regression.

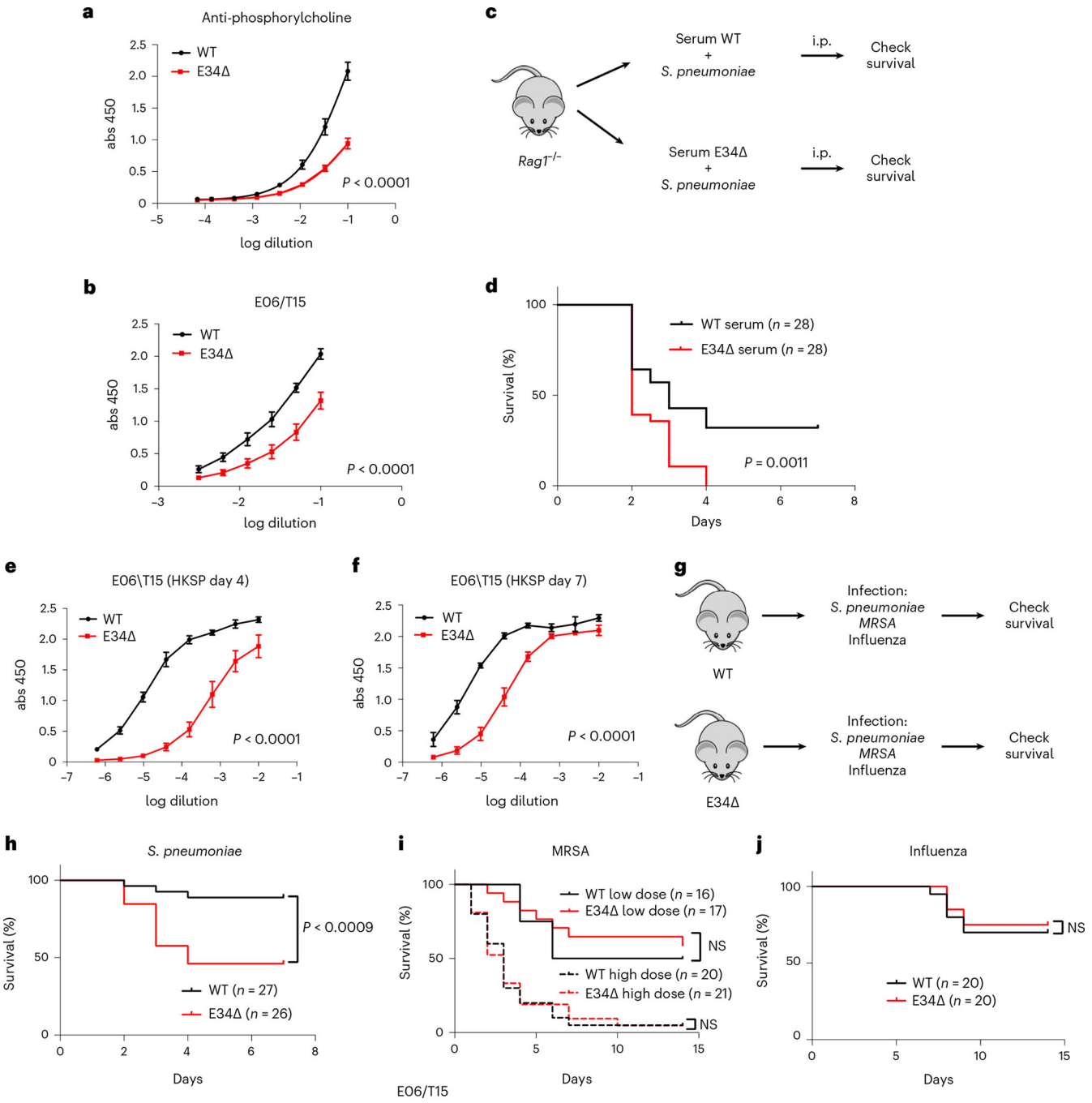

Fig. 8 |. Impaired natural antibody responses and increased *S. pneumoniae* lethality in E34Δ mice.

a, Quantification of anti-phosphorylcholine antibodies using ELISA for serum isolated from WT and E34Δ mice ($n = 4$) presented as mean ± s.e.m. **b**, Quantification of EO6/T15 IgM antibodies using ELISA for serum isolated from WT ($n = 6$) and E34Δ mice ($n = 7$) presented as mean ± s.e.m. **c**, Infection strategy to assess impact of changes in anti-phosphorylcholine antibody levels in mice survival. **d**, Effects on lethality after transfer of a mixture of serum derived from WT and E34Δ mice and *S. pneumoniae* (50 colony-

forming units) into *Rag1*$^{-/-}$ mice (n = 3). **e**, Quantification of EO6/T15 IgM using ELISA for serum isolated from WT and E34Δ mice after i.p. immunization with 10^8 heat-killed *S. pneumoniae* (HKSP) (n = 3). Serum was collected 4 d post-inoculation. Data are presented as mean ± s.e.m. Significant differences between WT and E34Δ ELISA data were determined using an extra sum-of-squares F test. **f**, Quantification of EO6/T15 IgM using ELISA for serum isolated from WT and E34Δ mice after i.p. immunization with 10^8 HKSP (n = 3). Serum was collected 7 d post-inoculation. Data are presented as mean ± s.e.m. Significant differences between WT and E34Δ ELISA data were determined by an extra sum-of-squares F test. **g**, Strategy to assess lethality of WT and E34Δ mice after infection with *S. pneumoniae* (50 colony-forming units), MRSA (low dose = 0.8×10^8 and high dose = 1.7×10^8 colony-forming units) and influenza virus (50 PFU). Data are derived from three independent experiments for *S. pneumoniae* and two independent experiments for MRSA and influenza. **h**, Lethality of WT and E34Δ mice after intravenous infection with *S. pneumoniae* (50 colony-forming units). **i**. Lethality of WT and E34Δ mice after intravenous infection with MRSA (low dose = 0.8×10^8 and high dose = 1.7×10^8 colony-forming units). **j**, Lethality of WT and E34Δ mice after intranasal infection with influenza virus. To analyze ELISA data, a four-parameter logistic (4PL) curve regression model was used. Significant differences between WT and E34Δ ELISA data (**a**, **b**, **e**, **f**) were determined using an extra sum-of-squares F test. Significant differences in survival in **d** and **h**–**j** were analyzed using a log-rank (Mantel–Cox) test. abs, absorbance; i.p., intraperitoneal; NS, not significant.